*remote sensing*

MDPI

*Article*

# Interpretation of the Spatiotemporal Evolution Characteristics of Land Deformation in Beijing during 2003–2020 Using Sentinel, ENVISAT, and Landsat Data

**Shuangcheng Zhang [1,2,*], Yafei Zhang [1], Jing Yu [1], Qianyou Fan [1], Jinzhao Si [1], Wu Zhu [1] and Mingxin Song [3]**

[1] School of Geology Engineering and Geomatics, Chang'an University, Xi'an 710054, China; 2020126037@chd.edu.cn (Y.Z.); 2019226003@chd.edu.cn (J.Y.); 2020026013@chd.edu.cn (Q.F.); 2020126029@chd.edu.cn (J.S.); zhuwu@chd.edu.cn (W.Z.)
[2] State Key Laboratory of Geo-Information Engineering, Xi'an 710054, China
[3] Xi'an Institute of Prospecting and Mapping, Xi'an 710054, China; 2018226008@chd.edu.cn
* Correspondence: shuangcheng369@chd.edu.cn

**Abstract:** Since the 1930s, due to the rapid development of the city and the increase of population, the demand from Beijing residents for water resources has gradually increased. Land deformation in the Beijing Plain is a serious issue. In order to warn of, and mitigate, disasters, it is urgently necessary to obtain the latest rate, extent, and temporal evolution of land subsidence in Beijing. Firstly, the temporal and spatial distribution characteristics of land deformation in Beijing during 2003–2020 were unveiled using the time-series interferometric synthetic aperture radar (InSAR) technique and two different satellite datasets, sentinel-1a/1b and ENVISAT ASAR. By means of combining calibration of InSAR results with the global positioning system (GPS), we studied the evolutionary process of long-term land subsidence in Beijing. The precision of our InSAR annual subsidence results is less than 10 mm. Land subsidence in Beijing is unevenly distributed, and so five main land subsidence zones were monitored. The time-series results showed that the rate of land subsidence rate continued to increase from 2003 to 2015, but has gradually shown a slowing trend from 2015 to 2020. Further, we used the quadratic polynomial fitting method to interpolate the time-series deformation results from 2010 to 2015, and compared these with GPS. The results demonstrated that although the InSAR observation method is not strictly registered with GPS in time, its deformation trend is consistent. In addition, the calibrated long time-series was consistent with the three deformation stages of land subsidence evolution in Beijing. Finally, we analyzed the deformation information obtained by InSAR technology in combination with land use type data, precipitation and groundwater data. The results demonstrated that the central area is mostly stable, and land deformation in the northeast is obvious and uneven. In addition, land use type and precipitation have little influence on land subsidence. Changes in land subsidence were closely related to changes in groundwater level, and seasonal variations in deformation correlated with precipitation.

**Keywords:** land subsidence; dataset calibration; quadratic polynomial fitting; spatiotemporal evolution characteristics



**Citation:** Zhang, S.; Zhang, Y.; Yu, J.; Fan, Q.; Si, J.; Zhu, W.; Song, M. Interpretation of the Spatiotemporal Evolution Characteristics of Land Deformation in Beijing during 2003–2020 Using Sentinel, ENVISAT, and Landsat Data. *Remote Sens.* **2022**, *14*, 2242. https://doi.org/10.3390/rs14092242

Academic Editors: Francesca Ardizzone and Michele Saroli

Received: 13 March 2022
Accepted: 5 May 2022
Published: 7 May 2022



## 1. Introduction

Beijing has an extensive geopolitical history and cultural diversity. It is the political, cultural, and international communication capital of China. Social, economic, and urban development have been rapidly increasing in Beijing. In addition, Beijing has been affected by land subsidence since 1935 [1]. In the 1970s, rapid, large-scale, and concentrated land subsidence was observed. Consequently, new subsidence areas, such as Changping, Shunyi, and Daxing, have gradually appeared. Land subsidence is a local descending movement caused by consolidation and compression of the underground loose strata under the influence of human engineering economic activities. It is also the main regional environmental

geological disaster in China [2]. Therefore, analyzing long-term land subsidence in Beijing is necessary.

With acceleration in urbanization a number of technologies have been commonly used to monitor surface subsidence in Beijing: precise leveling surveys [3], global positioning system (GPS) [4], interferometric synthetic aperture radar (InSAR) [5] and other technologies. Among these, leveling has several advantages, including high precision, advanced technology, and reliable results. However, it can only reflect the overall situation of surface deformation in Beijing, and requires permanent observations which can be time-consuming and labor-intensive. GPS technology can provide high-precision geographical coordinates, which can be used to monitor global and regional crustal deformation and land subsidence. However, GPS technology can only provide a limited number of discrete points for land subsidence monitoring, has a small monitoring range, and cannot obtain real-time and macroscopic deformation monitoring results in most cases. In contrast, InSAR, a novel method of determining land subsidence, can provide high-precision three-dimensional terrain information and small-scale land deformation information [6–10]. It greatly reduces costs and labor, and provides risk analysis and early warning signals during rapid urban development [11–15]. In contrast to conventional measurements, it can provide land subsidence results with centimeter-level, or even millimeter-level, accuracy over a large region [16]. The conventional differential interferometry synthetic aperture radar (D-InSAR) method was based on individual interferogram to obtain land subsidence [17]. However, it does not capture changes in deformation rate within the study area. In addition, changes in atmospheric conditions, satellite orbit errors and digital elevation model (DEM) errors also significantly reduce the accuracy of D-INSAR measurements. The Small Baseline Subset (SBAS) technique, proposed by Berardino et al. [18,19], can continuously and stably monitor the land surface for a long period in a large area with a specific revisit period, thereby minimizing the limitations of conventional measurement methods [20]. Regarding land subsidence monitoring in Beijing using the InSAR method, some annual InSAR deformation results have been exhibited in recent years. Shi [21], Yuan [22], Zhou [23], Li [24] and Pan et al. [25]. obtained the deformation sequence of Beijing for a long time period using SBAS-InSAR technology. In addition, many experts and scholars have conducted relevant studies on the spatiotemporal evolution of surface deformation in Beijing and its genesis mechanism. Zhou et al. [26] used ENVISAT ASAR and RadarSAT-2 data, and found several settlement funnels in the north and east of Beijing. Further, Du et al. [27] used ALOS data, and found that the subsidence rate in northern Beijing accelerated from 2007 to 2016. Liu et al. [28] used ENVISAT ASAR and RadarSAT-2 data and SBAS-InSAR technology to obtain vertical deformation characteristics of Beijing during 2003–2013. Muhetaer et al. [29], Yang [30], and Ng [31] analyzed the spatiotemporal distribution characteristics of land deformation in Beijing using time-series InSAR and GPS technologies. Hu et al. [32] analyzed development and changes in land deformation and their relationship with geological faults in Beijing from 2015 to 2017 using an atmospheric estimation model time-series analysis method. Further, Zhou et al. [33] introduced the machine learning approach to analyze the influence of groundwater, compressible layer thickness and other influencing factors on land deformation. Previous studies either identified land subsidence stages, by the analysis of individual interferograms based on conventional InSAR method, or detected land subsidence in a limited time, by SBAS-InSAR. New data and more advanced InSAR techniques are demanded to gain the latest rate, scope of activity, and temporal evolution of ground deformation in Beijing. In addition, there are some time gaps between different SAR datasets.

To better study long-term evolution of land deformation in Beijing, we need to continuously update the time series of different sensor deformations. SAR images provided by a single radar satellite are insufficient to reflect the long-term evolution of land subsidence, thus we need to combine the Sentinel satellite with others to update the time series of different sensors' monitoring of deformation. Samsonov [34] and Pepe et al. [35] used a singular value decomposition algorithm to fuse multi-satellite time-series data

with time overlap data, further fusing the vertical deformation time-series of ENVISAT ASAR and COSMO -SkyMed using the consolidation settlement model, thus realizing the deformation time series over a long time period. Based on the Sentinel-1A/1B, and ENVISAT ASAR datasets, and GPS measurements since 2003, our study aimed to acquire the spatial and temporal distribution characteristics of land subsidence in Beijing from 2003 to 2020 provided by advanced InSAR technology. First, the interferograms of two different InSAR datasets are processed by SBAS-InSAR technology respectively, and time series deformation measurements from 2003 to 2020 are generated to reveal the temporal and spatial changes of land subsidence in Beijing. Second, combined with calibration of the InSAR results by GPS, we obtained the spatial and temporal changes of land subsidence in Beijing over nearly twenty years. In addition, the results were verified by the Mann-Kendall method. Finally, we discuss the correlation between land subsidence and land use type, groundwater, and precipitation. The rest of the manuscript is organized in the following way: Section 2 introduces the study area; Section 3 introduces the SBAS-InSAR algorithm, GNSS processing strategy and the data used for processing and verification; Section 4 introduces the temporal and spatial changes of land subsidence in different SAR datasets and the settlement results of fusion time series; and Section 5 introduces the relationship between land subsidence and land use type, groundwater level, precipitation, ground fissures and fault activity, Section 6 summarizes our conclusions.

## 2. Study Area

Beijing is located in northern China and north of the North China Plain, ad-jacent to Tianjin in the east and Hebei in the west. It has a total area of 16,412 km$^2$. The elevation of Beijing is high in the northwest and low in the southeast, with an average elevation of 43.5 m. Beijing is surrounded by mountains in the west, north and northeast, whereas the southeast region comprises a plain gradually sloping towards the Bohai Sea. Figure 1 shows the geographical location of Beijing. The depressions in the Beijing plain area are loose sediments with thicknesses of more than 1000 m, which are prone to ground fractures and land subsidence [36].

According to results from the Beijing earthquake station, the faults in the northeast mainly include Huangzhuang-Gaoliying fault and Shunyi's buried active fault, and the horizontal deformation of these faults is mainly dextral. However, the Sunhe-Nankou fault is a typical fault in the northwest; its horizontal deformation is mainly characterized by sinistral deformation [37]. The faults in the northeast and northwest reflect tectonic compression to a certain extent. In addition, some earthquakes in Beijing are mainly related to characteristics of the crustal structure and physical properties of the rocks. The fault structure has a significant controlling effect on quaternary sediments in the Beijing plain and is closely related to seismic activity. The quaternary tectonic activities have both inheritance and cenozoic factors, and the distribution of depositional centers is more complex than those in the northeast. The tertiary and tectonic activities in the northwest are more obvious. Studies have shown that spatial distribution of land deformation was consistent with that of the quaternary compressible layers in Beijing [38]. Land subsidence in the plain is more severe, and the frequency of land subsidence in Chaoyang, Shunyi, Tongzhou, Changping, Haidian and other areas in Beijing is higher and the degree of harm greater. More than half of the Beijing plain area is seriously affected by land subsidence [39].

The geological environment in Beijing is complicated. Therefore, combined with groundwater, geological information, land use type data, and the result of time-series SBAS, it is necessary to continuously monitor land subsidence in Beijing for a long time.

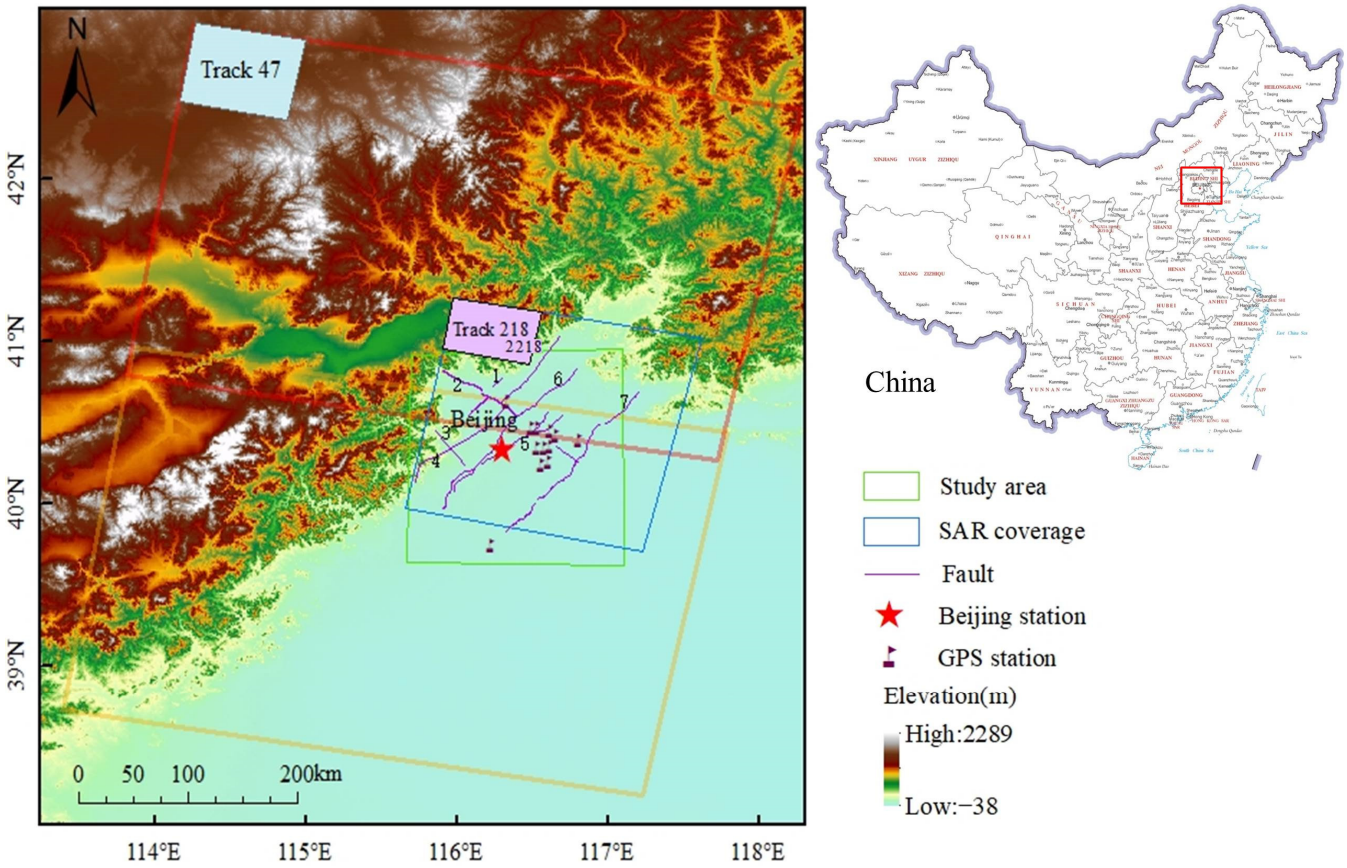


**Figure 1.** Study area geographical location and coverage of the Synthetic Aperture Radar (SAR) data. In the background is the shaded terrain-generated digital elevation model (SRTM DEM) of the Shuttle Radar Topography Mission. The red and yellow rectangles represent the coverage of sentinel-1 SAR data, the blue indicate coverage of ENVISAT ASAR data, and the green rectangle represents the location of the study area. The Beijing Plain is mainly controlled by northeast and northwest direction active faults. The northeast direction fault systems are composed mainly of the Xiaotang Mountain (1), Huangzhuang-Gaoliying (4), Tongxian-Nanyuan (5), Shunyi-Liangxiang (6), and Xiadian (7) faults. The northwest direction fault systems are composed mainly of the Nankou Sunhe (2) and the Yongding River (3) faults. The figure in the upper right corner shows the location of the study area in China. It can be downloaded from http://bzdt.ch.mnr.gov.cn/index.html, accessed on 12 January 2022. The part of the red rectangle in the map corresponds to the figure on the left.

## 3. Materials and Methods

### *3.1. SAR Images*

ENVISAT and Sentinel-1A/1B image data of Beijing were used to monitor land subsidence, and to analyze the spatiotemporal evolution characteristics of land subsidence in Beijing. ENVISAT ASAR is a polar-orbiting Earth observation satellite launched by the European Space Agency (ESA) in 2002, while Sentinel-1A/1B is an active radar imaging satellite launched by the ESA in 2014. In total, our study used 40 SAR images from the ENVISAT ASAR satellite from 2003 to 2010, and 90 SAR images from Sentinel-1A/1B satellite from 2015 to 2020. Both datasets had a VV polarization model. The specific imaging parameters are listed in Table 1, and the time span of the SAR dataset used in this study is shown in Figure 2. The processed SAR datasets span the entire time interval between June 2003 and December 2020. Due to the absence of comprehensive SAR datasets, there is a significant temporal gap (about five years) between the available ENVISAT and Sentinel datasets. The spatiotemporal baseline diagrams of the two data types are shown in Figure 3.

**Table 1.** Information of the SAR dataset.

| Sensor | ENVISAT ASAR | Sentinel-1A/1B |
|---|---|---|
| Band | C | C |
| Wavelength (cm) | 5.5 | 5.56 |
| Heading (°) | −164 | −166 |
| Track | 2218 | 47 |
| Polarization | VV | VV |
| Orbit directions | Descending | Descending |
| Number of images | 40 | 90 |
| Data range | 18 June 2003–29 September 2010 | 24 January 2015–22 January 2021 |
| Incidence angle (°) | 22.8 | 33.9 |

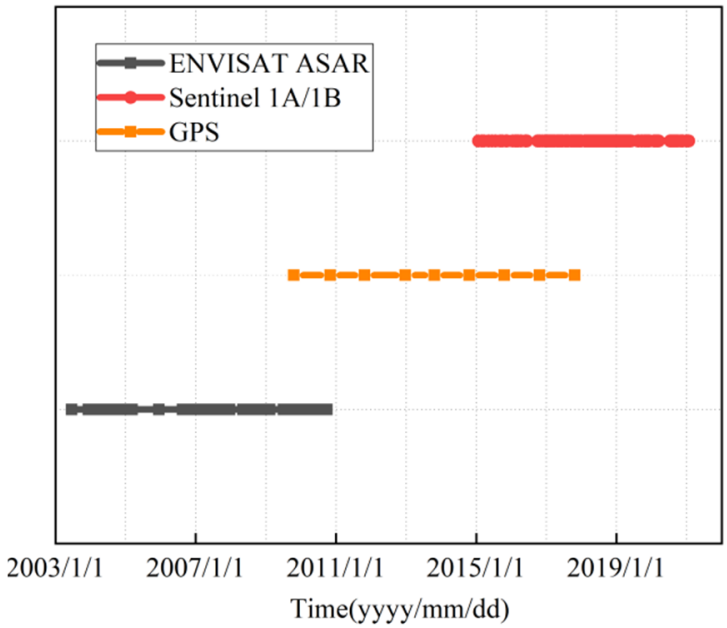


**Figure 2.** Time span of the SAR datasets and GPS measurement.

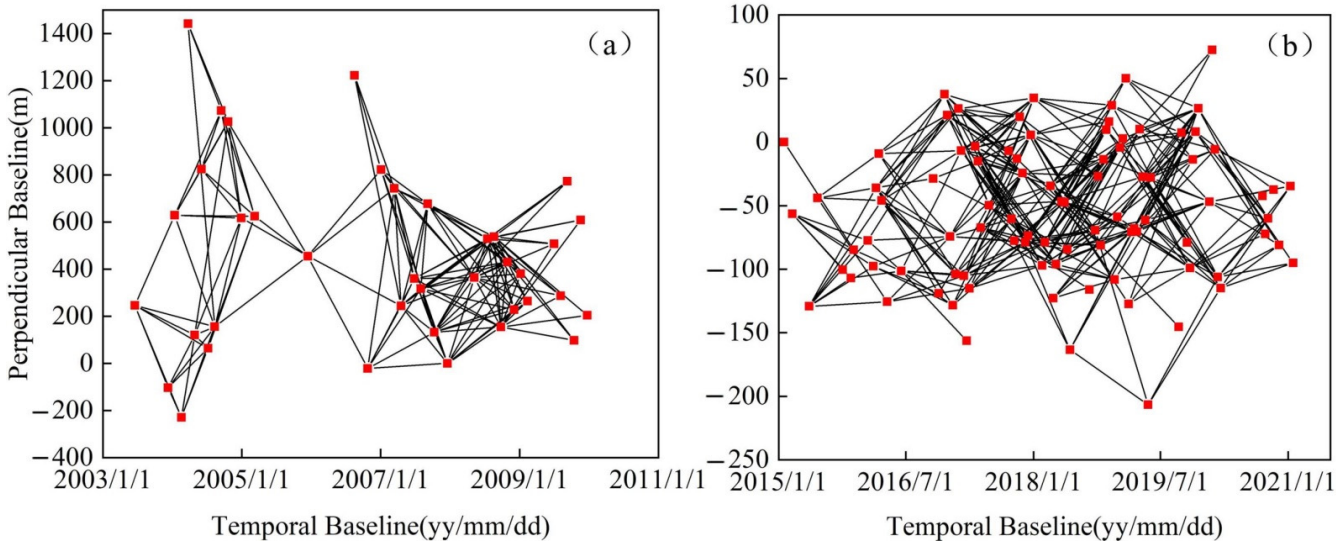


**Figure 3.** Temporal and perpendicular baseline maps of (**a**) ENVISAT ASAR and (**b**) Sentinel-1A/1B.

### 3.2. Other Datasets

Digital elevation model (DEM) data, having a spatial resolution of 30 m and provided by the National Aeronautics and Space Administration (NASA) Shuttle Radar Topography Mission (SRTM), were used in this study. In addition, the five-year interval land use data (spatial resolution: 30 m) from 2005 to 2020, provided by Landsat data through the Google Earth Engine (GEE) platform [40], were used. Groundwater exploitation and depth data were provided by the Beijing Water Authority, and precipitation data of the meteorological station were provided by the National Oceanic and Atmospheric Administration (NOAA). Groundwater exploitation and depth data can be downloaded from http://swj.beijing.gov.cn/, accessed on 10 February 2022. Precipitation can be downloaded from https://www.ncei.noaa.gov/maps-and-geospatial-products, accessed on 10 February 2022. Moreover, the data from 12 global positioning system monitoring sites in Beijing, from 2009 to 2020, were acquired by the Beijing Institute of Geological & Prospecting Engineering in China. Each monitoring site had 12 data periods, and each monitoring site was a bedrock point. The distribution of monitoring points is shown in Figure 1.

### 3.3. Land Subsidence Monitoring Using SBAS-InSAR

The principle of SBAS-inSAR technology is to combine all SAR data into several small sets by setting certain spatiotemporal baseline thresholds, with smaller baselines within the sets and larger baselines between the sets. Finally, through the least square solution within the set and the singular value decomposition method between the sets, the joint solution result of the surface deformation information of the whole time-series is obtained [41,42]. In this way the data utilization rate is improved to overcome the incoherent problem of image information. In addition, the influence of DEM error on deformation measurement can be reduced.

Assuming that there are $N$ + 1 SAR images covering the same area and the time series is $(t_0, \cdots, t_N)$, $M$ differential interferograms can be obtained under the condition that the spatiotemporal threshold is satisfied. Let the acquisition times of the primary and secondary images of the differential interferogram $i$ be $t_B$ and $t_A$, respectively, and $t_B > t_A$. Thus, the differential interference phase generated by SAR images at pixels $(x, y)$ of $t_A$ and $t_B$ can be expressed as:

$$\delta_{\varphi_i}(x,y) = \varphi(t_B,x,y) - \varphi(t_A,x,y) \approx \varphi_{def,i}(x,y) + \varphi_{topo,i}(x,y) + \varphi_{atm,i}(x,y) + \varphi_{noise,i}(x,y) \quad (1)$$

where, $(x, y)$ are azimuth direction and distance direction coordinates, $\varphi(t_B, x, y)$ and $\varphi(t_A, x, y)$ is the image phase generated by the differential interferogram phase, $\varphi_{def,i}(x, y)$ is the deformation phase caused by interference on the land displacement between $t_A$ and $t_B$, $\varphi_{topo,i}(x, y)$ is the topography phase error caused by topographic undulation, $\varphi_{atm,i}(x, y)$ is the atmospheric phase error, $\varphi_{noise,i}(x, y)$ is the random noise phase.

According to Equation (1), a set of equations including M equations and N variables can be obtained [18]:

$$\delta_\varphi = A\varphi \quad (2)$$

where $\delta_\varphi$ is the matrix formed by $M$ differential interferogram phase, $\varphi$ is the matrix of the deformation phase to be determined by an image on $N$ SAR. $A$ is an $M \times N$ matrix, each row corresponds to an interference pair. When the number of small baseline subsets is one, $A$ is the full rank matrix, and its least square solution is:

$$\hat{\varphi} = [(A^T A)^{-1} A^T] \cdot \delta_\varphi \quad (3)$$

When the number of small baseline subsets is greater than 1, $A$ is a rank-deficient matrix and the rank deficient is $N - L + 1$. $A^T A$ is a singular matrix, and there are infinite solutions to the equation. To solve this problem, the equation must be transformed into the phase average change rate in the sense of the minimum norm, and the pseudo-inverse

matrix can then be obtained by the singular value decomposition method [43]. Let the parameter to be solved be expressed as:

$$v = \left[ \frac{\varphi_1 - \varphi_0}{t_1 - t_0}, \cdots, \frac{\varphi_N - \varphi_{N-1}}{t_N - t_{N-1}} \right]^T \tag{4}$$

where the value of $\varphi_0$ is zero. It can be further obtained as:

$$\delta_{\varphi_i} = \sum_{i=tS_i+1}^{tM_i} v(t_i - t_{i-1}), \quad i = 1, \cdots, M \tag{5}$$

where $tM_i$ and $tS_i$ respectively represent the acquisition time of the master and slave image corresponding to the interferogram $i$. For $M$ differential interferogram, equations can be formed:

$$B \cdot v = \delta_\varphi \tag{6}$$

where, $B$ is a $M \times N$ matrix corresponding to the unknown vector. For each row element in $B$, the value of $B(j,i)$ is $t_{i+1} - t_i$. Everything else in the matrix is 0. Subsequently, singular value decomposition was performed on matrix $B$, the value of which is $USV^T$ [44], where $U$ is an $M \times N$ orthogonal matrix, $S$ is a $M \times N$ diagonal matrix, and $V$ is an $N \times N$ orthogonal matrix. According to least squares, the phase change rate can be expressed as:

$$v = VS^{-1}U^T\delta_\varphi \tag{7}$$

### *3.4. GPS Processing Strategy*

In order to obtain the results of high-precision positioning of GNSS data, we used the GAMIT/GLOBK10.7 software package developed by the Massachusetts Institute of Technology (MIT) and Scripps Institution of Oceanography. GAMIT/GLOBK software has the characteristics of high precision, is a free and open source for scientific research institutes, has continuous upgrading and updating, and has been widely used in high-precision GNSS data processing at home and abroad [45]. Using precise ephemeris and high precision starting points, the relative accuracy of the baseline solution can reach about 10 mm, and the accuracy of the short baseline solution can be better than 1 mm [46]. The data processing procedure of GPS measurements include observation data preprocessing, GPS baseline calculation, GPS network adjustment, and extraction of GPS station elevation change information [47]. Firstly, prior to high-precision processing of GPS data, preprocessing the original GPS observation data was necessary. We used GPS observation data quality analysis software (TEQC) to analyze the quality of GPS original observation data. Secondly, we converted the qualified GPS data into RINEX standard format data as the input data of the high-precision GPS data processing software GAMIT/GLOBK. Thirdly, combined with the data of the IGS global tracking station, we used GAMIT/GLOBK 10.7 software to calculate the baseline of GPS survey data, and adopted the double difference relative positioning mode for baseline calculation [48]. In addition, in order to ensure the accuracy of GPS baseline calculation, we used the IGS precise ephemeris and atmospheric correction model to eliminate errors in orbit and signal propagation and ensure the accuracy of GPS baseline calculations. The adjustment principle of GLOBK software can be found in references [49,50]. Fourthly, we obtained the three-dimensional coordinates of the frame points with the high-precision GPS elevation change monitoring software package (HPGP-SADJ). In addition, the International terrestrial Reference Frame (2008) was adopted in GPS monitoring of land subsidence in Beijing from 2009 to 2020 to reduce the error caused by coordinate conversion calculation. Finally, based on the network adjustment results of GPS measurement points, and the GPS monitoring results, we obtained the settlement amount and development trend of each GPS measurement point of land subsidence in Beijing.

### *3.5. Dataset Calibration for Different Platforms*

While processing ENVISAT ASAR and Sentinel-1A/1B data using SBAS-InSAR technology, selecting the same coordinates of unwrapped reference points of the two datasets is necessary. The specific operational process for processing involves transforming the same selected geographical coordinates into phase coordinates. Due to the deformation information captured by ENVISAT and Sentinel in different spatial regions, it was necessary to extract overlapping regions of the two datasets. To obtain a development trend of land subsidence over the period 2003 to 2020, we projected LOS direction deformation from different sensors to the vertical direction and geocoded them in the same geographic coordinate system. By using continuous GPS measurement and quadratic polynomial interpolation, we referenced two measurement data to the same location and corrected the offset in time to obtain GPS and InSAR observation data in the same temporal and spatial reference frame.

Before calibration, due to differences in the incident angle and resolution of different satellite data, land subsidence in the Beijing area was mainly vertical, and the deformations in the east–west and south–north directions were relatively small [51]. Therefore, the LOS deformation results can be projected in the vertical direction using the following formula:

$$V_{Vertical} = \frac{V_{LOS}}{cos\theta} \quad (8)$$

where $\theta$ is the SAR satellite incidence angle. Notably, before the LOS deformation results are projected, we need to resample the deformation acquired by different sensors to have the same spatial resolution.

## 4. Results

### *4.1. Spatiotemporal Characteristics of Land Subsidence and Reliability Analysis*

To obtain land subsidence information in Beijing from 2003 to 2020, we processed SAR images from two different datasets employing SBAS-InSAR technology to obtain the annual average deformation rate chart and cumulative deformation chart along the line of sight (LOS) in Beijing during 2003–2010 and 2015–2020 (Figure 4). Figure 4a,b show annual average deformation rate during 2003–2010 and 2015–2020, whereas Figure 4c,d show the cumulative subsidence during 2003–2010 and 2015–2020. The deformation result was positive when the ground objects moved closer to the satellite. Conversely, the deformation result was negative when the ground object moved away from the satellite. Here, the positive value in blue indicates movement towards the satellite (representing lifting), and the negative value in red indicates movement in a direction away from the satellite (representing deformation). Due to the deformation information being captured by ENVISAT and Sentinel in different spatial regions, it was necessary to extract overlapping regions of the two datasets.

The spatial evolution process indicated that the distribution of land subsidence in Beijing was not uniform. The deformation in the central Beijing plain area was relatively small, and the land subsidence in the northeast was more severe. Subsidence was mainly observed in Changping, Haidian, Chaoyang, Shunyi and Tongzhou districts. Chaoyang, located in the northeast of Beijing, and Tongzhou showed the most severe subsidence. Furthermore, the subsidence of Chaoyang and Tongzhou districts tends to be contiguous. In addition, the deformation rate in Beijing during 2003–2010 ranged from −128 mm/year to 3 mm/year, and the maximum cumulative deformation was −808 mm, which was located in Chaoyang. The average deformation rate in Beijing during 2015–2020 ranged from −135 mm/year to 12 mm/year, with the maximum cumulative deformation being −734 mm. The maximum cumulative deformation was also observed in Chaoyang, Beijing.

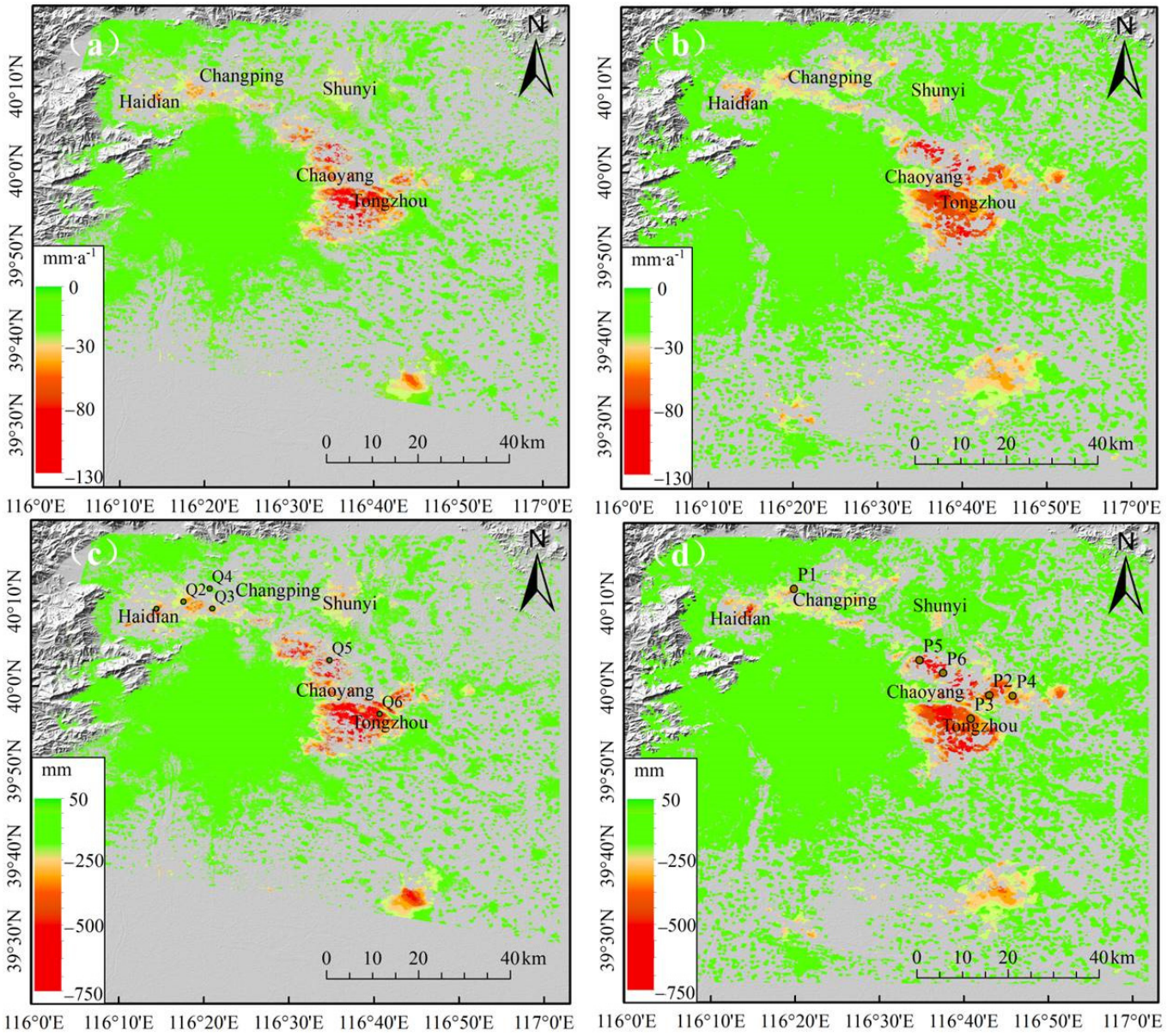


**Figure 4.** Deformation results of land subsidence along the LOS in Beijing during 2003–2010 and 2015–2020. Mean deformation velocity during 2003–2010 (**a**) and 2015–2020 (**b**). Cumulative deformation during 2003–2010 (**c**) and 2015–2020 (**d**). Note: Q1–Q6 (**c**) and P1–P6 (**d**) represent the extracted deformation feature points in typical subsidence area. The black marks in the figure are mainly deformation zones. The colored dots from green to red represent InSAR values.

In addition, to verify the reliability and accuracy of the deformation results, 35 GPS measurements were collected for verification. Due to the InSAR deformation result mainly reflecting deformation along the LOS direction [52], according to the heading and incident angle of the pixels corresponding to the GPS point, the GPS deformation result was uniformly projected to the LOS direction for checking of accuracy. GPS deformation in the line of sight can be expressed as

$$d_{\mathrm{GPS}} = \sin\theta \times \sin\left(\alpha - \frac{3\pi}{2}\right) \times d_x + \sin\theta \times \cos\left(\alpha - \frac{3\pi}{2}\right) \times d_y + \cos\theta \times d_z \qquad (9)$$

where, $\alpha$ is the satellite heading angle and $\theta$ is the radar incidence angle. $d_x$, $d_y$ and $d_z$ are the deformation of GPS in the three-dimensional direction, respectively.

There are three methods to verify the comparison between GPS measurement values and InSAR deformation results, which are point-to-point verification, point-to-surface verification, and point-to-line verification. In order to quantitatively evaluate the deformation monitoring accuracy obtained by InSAR and GPS, point-to-point verification was adopted to verify accuracy. In order to highlight the correlation of deformation between InSAR and GPS, we compared InSAR-derived deformation rates with GPS deformation results in the LOS direction (Figure 5). The difference between the deformation results of InSAR and GPS is less than 10 mm/a, and the root mean square error is 4.6 mm/a. In addition, the correlation between INSAR and GPS is high with a correlation value of about 0.9. The reliability of InSAR monitoring results is illustrated.

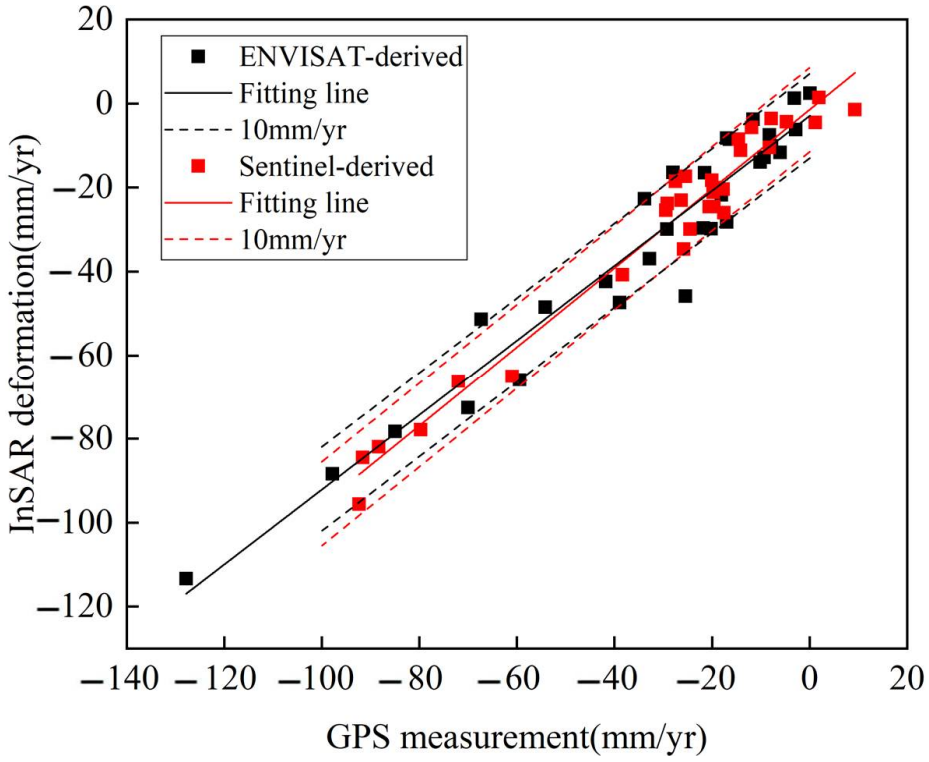


**Figure 5.** Correlation between GPS measurements and annual LOS deformation results of InSAR. Black scatter points are the ENVISAT-derived results, and black straight line is the line fitted by ENVISAT-derived results and GPS. Red scatter points are the sentinel-derived results, and red straight line is the line fitted by sentinel-derived results and GPS.

### *4.2. Time Series Land Subsidence*

To better analyze the long-term evolution characteristics of land subsidence in Beijing, six deformation feature points at different positions were extracted from the subsidence funnel in the accumulated deformation charts for 2003–2010 and 2015–2020. The location distribution of each feature point are shown in Figure 4b,d. A time-series deformation analysis was performed on the extracted feature points and the corresponding results are shown in Figure 6. Moreover, since only Gaussian noise is permitted in deformation time series, it is necessary to correct atmospheric error, orbit error and DEM error phase.

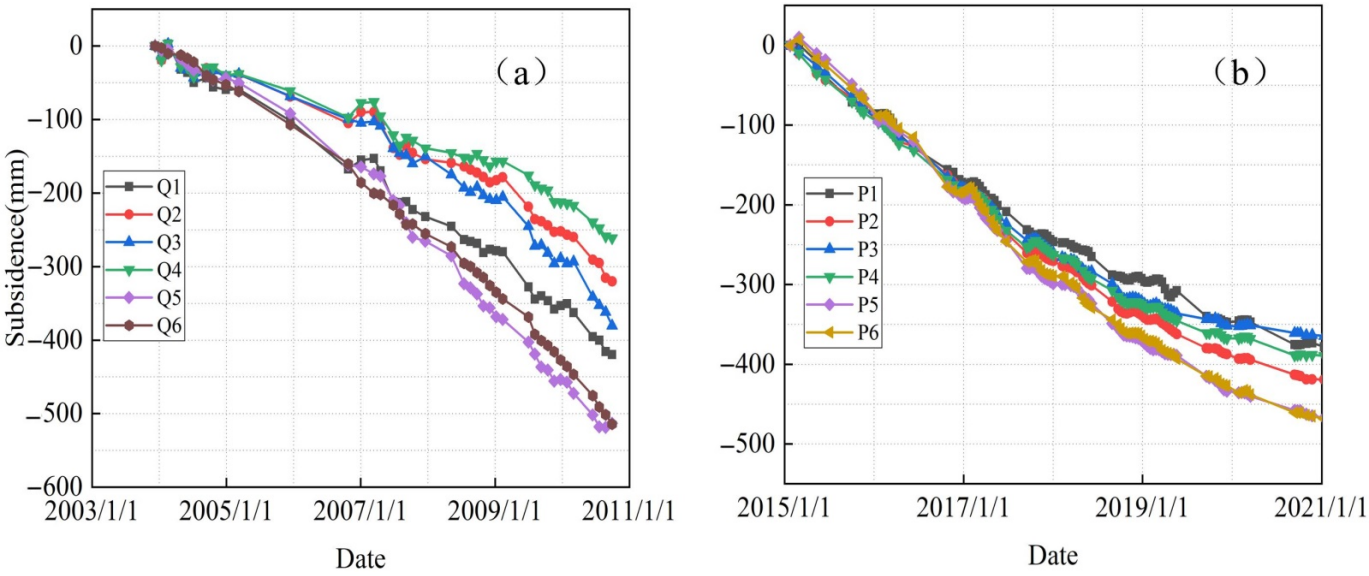


**Figure 6.** Time-series deformation of typical feature points from (**a**) 2003–2010 and (**b**) 2015–2020.

The time-series of the extracted feature points during 2003–2010 and 2015–2020 showed nonlinear subsidence at different velocities (Figure 6). From 2003 to 2010 (Figure 6a), land subsidence along the LOS in Beijing continued to increase, and its land deformation rate also increased, with the maximum accumulative deformation amount reaching −514 mm. The deformation was relatively small from 2003 to 2005. After 2006, the amount of land subsidence in Beijing increased gradually. Further, five observed deformation funnels expanded over approximately seven years in scale and number. The largest settlement center was located in Chaoyang. In addition, the time-series deformation diagram (Figure A1 in Appendix A) further demonstrates the formation process of settlement funnels from 2003 to 2010. From 2015 to 2020 (Figure 6b), land subsidence continued to increase. The subsidence in Chaoyang was the most severe, with the maximum accumulative deformation reaching −472 mm. The deformation changed slightly from 2015 to 2016, and then gradually increased from 2017 (Figure A2). Although the accumulated subsidence amount in Beijing continued to increase from 2005 to 2020, land subsidence showed a slowing trend from 2015 to 2020. In analyzing the time-series of each feature point, the time-series subsidence of Changping, Haidian, and Tongzhou, corresponding to the feature points Q1, Q2, Q3, Q4, P4, and P6, showed obvious seasonal characteristics. Considering the time series of the Q1 feature point as an example, land subsidence showed a rebound trend from October 2006 to October 2007, and subsequently continued to sink.

The development process of land subsidence in Beijing included three deformation stages: initial subsidence, serious subsidence and then gradual stability [53]. In the 1930s, land subsidence was found in Xidan and Dongdan of Beijing. With the expansion of industry in the city and over-exploitation of groundwater, several new settlement centers, such as Changping and Shunyi, emerged in Beijing. At the same time, problems, such as foundation settlement, buildings cracking and environmental pollution also occurred. It brought great financial loss and harm to urban construction and peoples' lives. In the case of vertical deformation, in order to analyze the development and change of land deformation in Beijing from 2003 to 2020, we projected LOS direction deformation from different sensors to the vertical direction and geocoded them in the same geographic coordinate system. In order to compare the time-series displacements of InSAR inversion with those from GPS, we generated a buffer 100 m radius around the GPS reference point. On this basis, we obtained the average displacement of all slow varying filtered phase (SFP) pixels in the buffer. After referring the two measurements to the same location, and correcting the offset in time, we obtained GPS and InSAR observations in the same temporal and spatial

reference frame. Finally, long-time and high-time resolution deformation time series were generated. The specific strategies were as follows:

The time-series results of the ENVISAT ASAR, GPS, and Sentinel-1A/1B data are shown in Figure 7. ENVISAT ASAR and Sentinel-1A/1B satellites have different incident Angles, spatial resolutions, and selected reference points. To address the problem of different reference points, we selected the same coordinate reference points during the SBAS-InSAR process. The ENVISAT ASAR and Sentinel-1A/1B data had incident angles of 22.8° and 33.9°, respectively. The deformation results obtained from the ENVISAT ASAR and Sentinel-1A/1B data were mainly vertical. Therefore, directly projecting the LOS deformation results obtained from ENVISAT ASAR and Sentinel-1A/1B data in the vertical direction was appropriate. Moreover, we resampled the deformation results obtained from the two datasets to 30m to ensure consistency of their spatial resolution. In this study, the time-series of the two feature points P3 (Figure 8a) and P5 (Figure 8b) were selected for calibration. Due to the fact that the ENVISAT satellite stopped operating around 2012 and the Sentinel satellite began operating in 2014, there is no temporal overlap between the two satellites. It was impossible to directly calibrate the time series deformation results obtained from ENVISAT ASAR and sentinel-1a/1b data. Therefore, we used GPS data and a polynomial fitting algorithm to calibrate the deformation results. The time-series deformations of the ENVISAT, Sentinel-1A/1B, and GPS data were referenced to the same position, and corrected and offset temporally. For the time-series deformation results obtained from InSAR, we selected deformation points within 100 m of the GPS monitoring points. ENVISAT ASAR and Sentinel-1A/1B data acquired on 10 December 2003 and 24 January 2015, respectively, were used as temporal data. Both had different temporal datum for obtaining deformation results; therefore, the temporal datum of ENVISAT ASAR and Sentinel-1A/1B had to be unified. The GPS data used for calibration were based on the image from 17 October 2009. Thus, long time-series deformation was acquired (as shown in Figure 8a,b) after rectifying the deformation results from 2003 to 2010 and 2015 to 2020. In the same time period, we found that, although the InSAR observation method is not strictly registered in time with GPS, its deformation trend was consistent. However, the time series was not continuous. To acquire the missing data from 2010 to 2015, we adopted quadratic polynomial fitting interpolation and a mean algorithm. The resultant deformation results for the long time-series are shown in Figure 8c,d. We used continuous GPS time series results to analyze the obtained results. It was found that the deformation trend of this result was consistent with GPS. In addition, the calibrated long time-series was consistent with the three deformation stages of land subsidence evolution in Beijing. This was mainly demonstrated through rapid land subsidence after the over-exploitation of groundwater in Beijing. As the South-to-North Water Transfer Project was implemented at the end of 2014, the rate of land subsidence gradually decreased, and gradually became stable. The maximum accumulative deformation amount at P5 reached −1368 mm. In addition, on comparing GPS deformation results from 2009 to 2020 with those of ENVISAT and Sentinel-1A/1B fused data, the temporal sequence results after supplementing were found to be consistent with GPS trends through visual interpretation. By observing the data supplemented by the quadratic polynomial fitting method and the mean value algorithm, the inflection point of land subsidence in Beijing was found to be located in the corresponding time span of the supplemented data. Quantitatively, the inflection point occurred around 2015. The result obtained by the Mann-Kendall method was consistent with the analysis results (Figure 9). The extent and magnitude of land subsidence are related to geological structures [54–56]. Since geological structural changes occur over a certain time period, the magnitude of land subsidence does not change quickly. However, the rate of land subsidence can change with changes in groundwater [57,58]. The South-to-North Water Transfer Project significantly reduced the amount of groundwater exploitation. Thus, based on the analysis of the actual scenarios, the inflection point could have occurred due to the implementation of this project, which slowed the deformation rate of land subsidence to a certain extent.

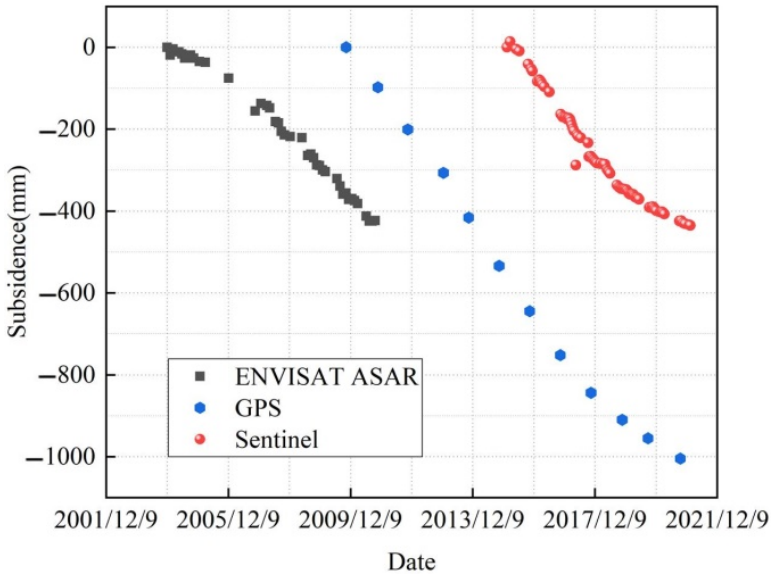


**Figure 7.** Time-series deformation results of typical feature points from 2003 to 2010.

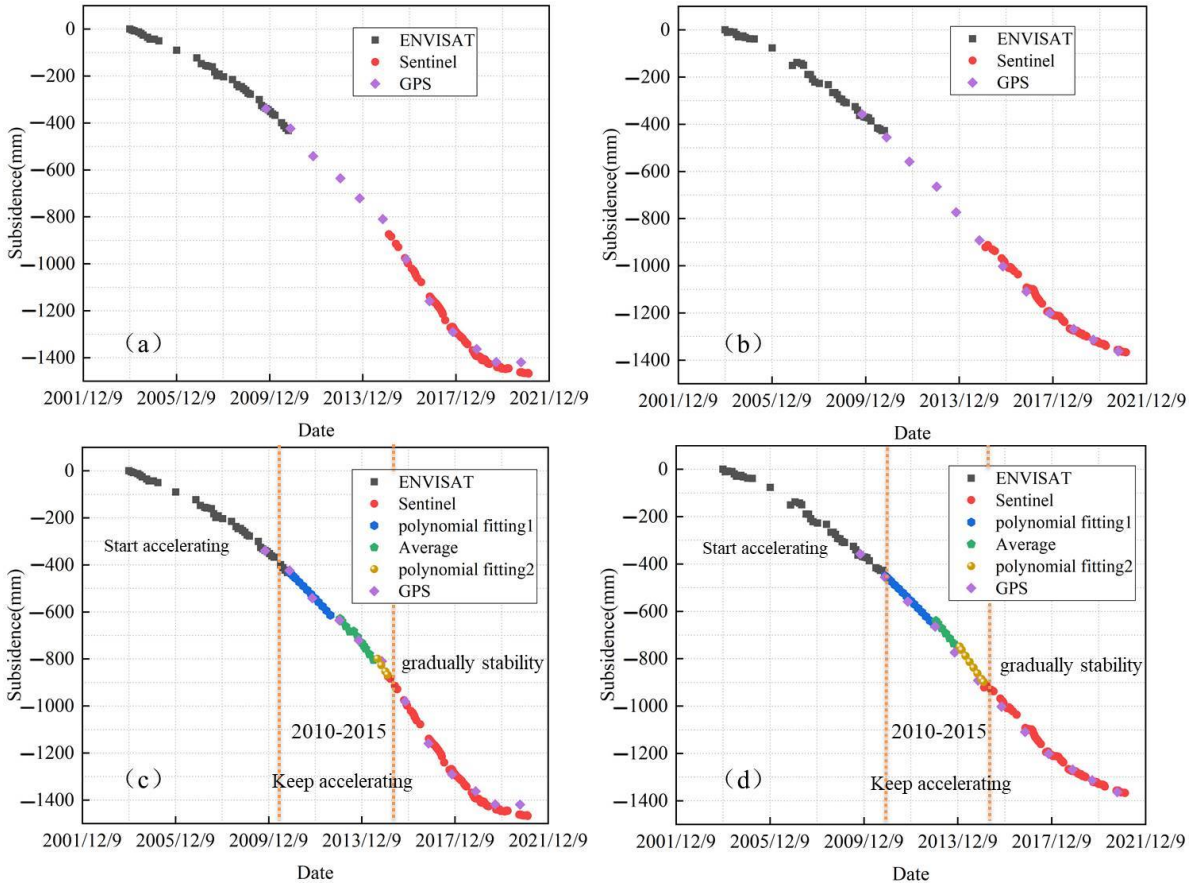


**Figure 8.** Comparison of the corrected time series settlement with GPS observation results: (**a**,**b**) are the corrected results of time series deformation at P3 station and P5 station, respectively. (**c**,**d**) are the supplemented results at P3 station and P5 station during 2010–2015.

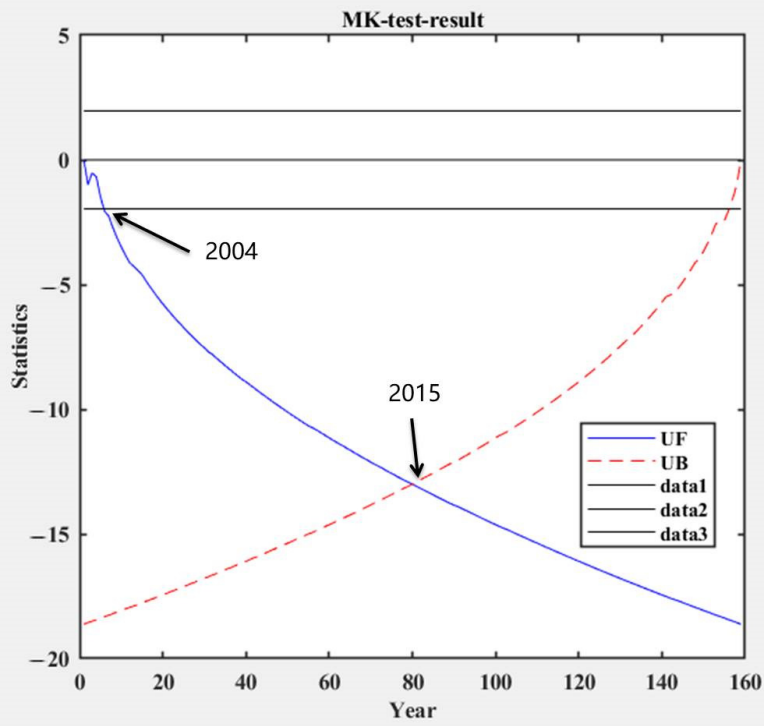


**Figure 9.** Mann-Kendall test result.

## 5. Discussion

### *5.1. Relationship between Land Subsidence and Land Use Type in Beijing during 2003–2020*

Land subsidence is a slow time-dependent subsidence process, which may have a slow and correlated response to land use and cover [59,60]. In order to explore the relationship between surface deformation and land use types in Beijing, we used previously obtained information of surface deformation rate from 2003 to 2020 to explore the evolutionary relationship between surface deformation and land use types in Beijing, based on land cover data.

With rapid urbanization, the proportion of construction land in Beijing is gradually increasing, whereas that of cropland is decreasing. To analyze the changes in land use types in Beijing over a long period of time we acquired the distribution data of land use types in Beijing from 2005 to 2020 over a five-year interval, and used ArcGIS software to perform simple operations, such as reclassification and superposition analysis. Figure 10 shows the land use types in Beijing from 2005 to 2020.

According to the distribution maps of land use types in 2005, 2010, 2015 and 2020, change of land use type in Beijing was obvious during the study period, especially the change in construction land. This type of land use is prone to land subsidence, because the loads of construction land and human activities lead to subsidence of construction land area [61]. The specific magnitude will be explained later.

In order to display the magnitude of change of land use types in detail during the study period, we calculated the area proportion of each land use type, and the corresponding statistical results are shown in Table 2. As time goes on, we found that construction land expanded in space, while cropland continued to decrease. The proportion of construction land increased by 5%, i.e., from 16.7% in 2005 to 21.8% in 2020. Further, during 2005–2020, the proportion of cropland decreased, whereas that of other land use types remained unchanged.

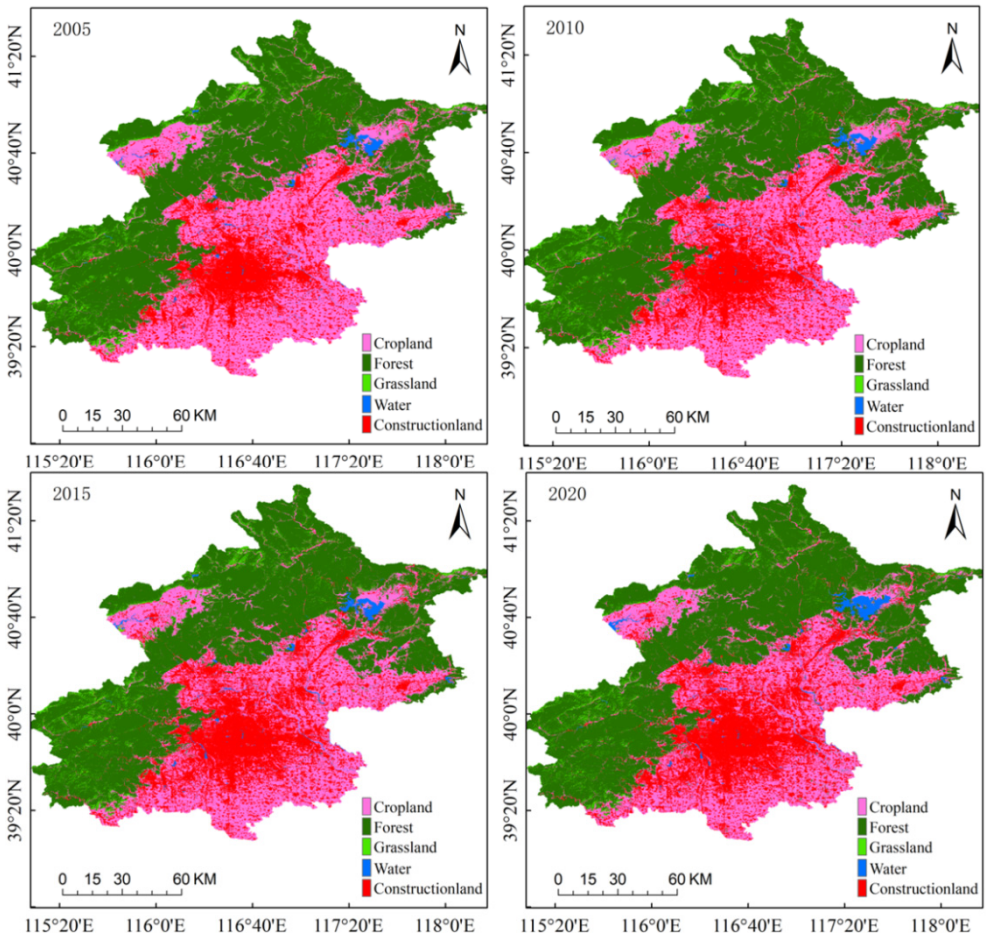


**Figure 10.** Land use types in Beijing from 2005 to 2020.

**Table 2.** Statistical results of different land types in Beijing (2005–2020).

| Land Use and Cover | Proportion of the Corresponding Area | | | |
|---|---|---|---|---|
| | 2005 | 2010 | 2015 | 2020 |
| Constructionland | 16.7% | 19% | 21.1% | 21.8% |
| Cropland | 31.2% | 28.6% | 26.5% | 25.6% |
| Forest | 47.6% | 47.8% | 48.4% | 48.8% |
| Grassland | 3.4% | 3.6% | 3% | 2.4% |
| Water | 1% | 1% | 1% | 1.4% |

Superposition analysis is a very important spatial analysis function in GIS. Under the unified spatial reference system, in order to analyze the relationship between evolution of land use type and land subsidence, we superimposed land use type data with land subsidence results from InSAR based on the 2005–2020 land use type data, having a resolution of 30 m. The land subsidence areas were mainly located in Changping, Tongzhou, Shunyi, Haidian and Chaoyang. Therefore, we analyzed the proportion of each land use type in these five land subsidence areas. The corresponding results are shown in Figure 11. The proportion of forest, grassland, and water in each of the five land subsidence areas was relatively small from 2005 to 2020, while that of cropland was the highest in 2005. However, over time, the proportion of cropland gradually decreased, and building density continued to increase, resulting in the proportion of construction land in each land subsidence area increasing, with the highest proportion observed in Tongzhou and Changping. The settlement is mainly concentrated in construction land, and is pretty small

in other land use types. Therefore, land subsidence is related to land use type. Compared with other land use types, construction land is more prone to land subsidence.

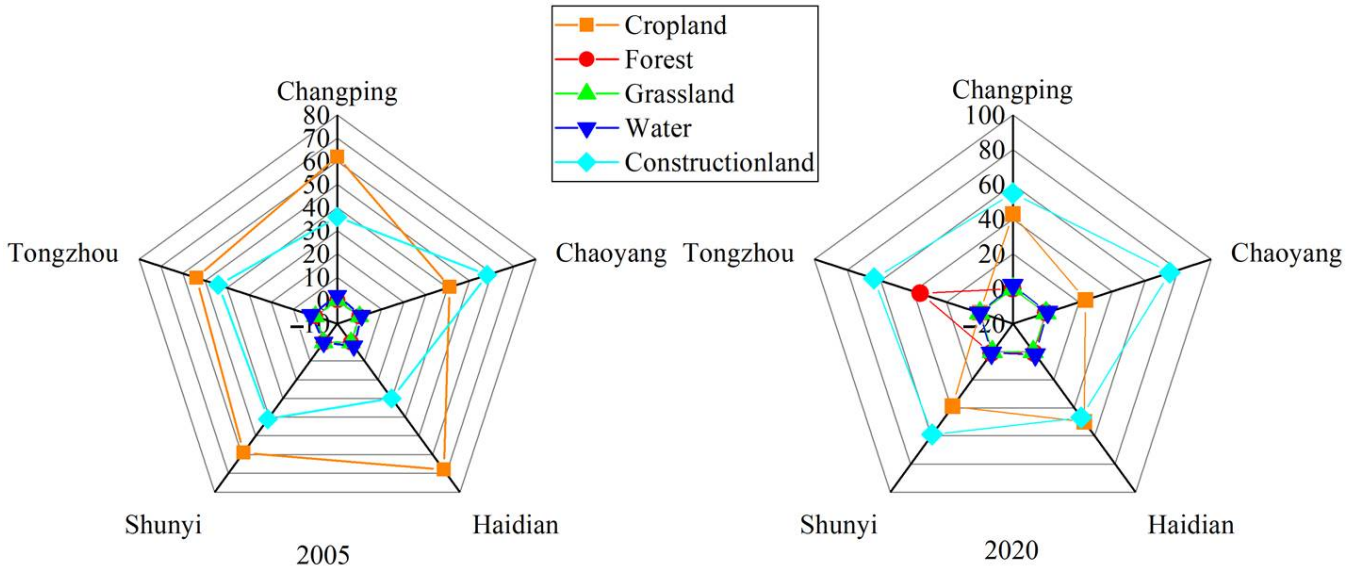


**Figure 11.** Proportion of land use types in the five subsidence areas of Changping, Haidian, Shunyi, Tongzhou, and Chaoyang.

Since changes in forest, grassland and water in the land subsidence area were pretty small, in order to better analyze the development and change of land subsidence from 2003 to 2020, we focused on the area of construction land and subsidence area in the study area during 2003–2020; the extent of change is shown in Figure 12. We also calculated the corresponding number of pixels. From 2005 to 2010, the proportion of construction land (the pixel count increased from 3,076,955 to 3,522,020) and land subsidence both showed an upward trend, and the change in both showed a positively correlation. It shows that construction land has an impact on land subsidence. Previous studies have proven that overexploitation of groundwater was the major cause of land subsidence in the Beijing plain. Groundwater is distributed in confined aquifers. Overexploitation of groundwater makes it difficult for the aquifer to bear the weight of its upper layer. Solari et al. [62] found that building load is a factor promoting high displacement rate. In the case of overexploitation of groundwater, the large-scale construction of buildings aggravates the rate of land subsidence. Therefore, the impact of construction land on land subsidence is closely related to massive exploitation of groundwater. After 2015, although the area of construction land continued to increase (the pixel count increased from 3,883,157 to 4,003,512), the proportion of land subsidence area decreased, which may be largely related to the South-to-North Water Transfer project, implemented at the end of 2014. In addition, Yang et al. [30] found that the use of long piles in high-rise buildings can effectively reduce the settlement, and increase of building load does not cause the same proportion of ground settlement. After effective measures were adopted in construction, the impact of construction land on land subsidence in Beijing was relatively small or even nothing. The reasons for the change of land subsidence1 rate with groundwater level will be explained in the next chapter.

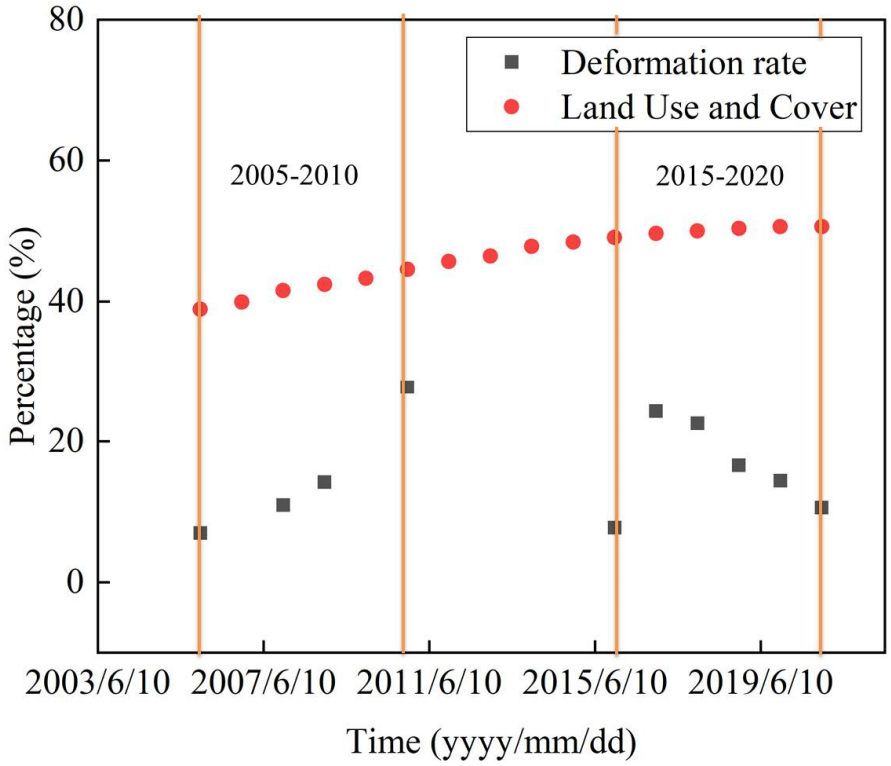


**Figure 12.** Change extent of construction land and deformation.

*5.2. Relationship between Land Subsidence and Groundwater in Beijing during 2003–2020*

According to previous studies, land subsidence and groundwater in Beijing are closely related [63]. We obtained groundwater depth and exploitation data from 2003 to 2020 from the Beijing Water Resources Bulletin [64], provided by the Beijing Water Authority. The corresponding land subsidence results were also analyzed. The results are shown in Figure 13.

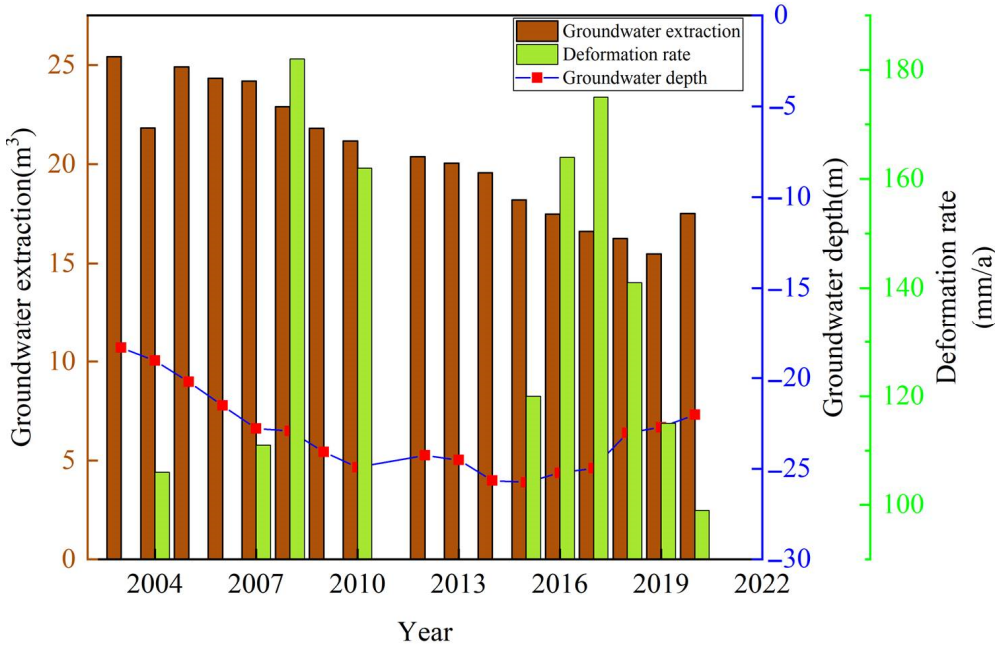


**Figure 13.** Evolutionary trend of groundwater data and deformation results from 2003 to 2020.

As shown in Figure 13, groundwater depth continued to increase from 2003 to 2010, and the annual average groundwater depth from 2013 to 2020 showed an important turning point around 2015; mainly reflected in slowing down of groundwater depth and a downward trend around 2015. Further, groundwater exploitation gradually decreased from 2003 to 2020, while the land subsidence rate increased between 2003 and 2010. Although groundwater exploitation decreased during this period, the decrease was not significant. Thus, the conclusion is that extreme exploitation of groundwater may have aggravated land subsidence. The changes in land subsidence rate from 2003 to 2015 in Beijing were not regular, but showed an overall increasing trend. The land subsidence rates were 106 mm/year in 2004 and 120 mm/year in 2015, and the deformation rate in 2015 was 14 mm/year, higher than that in 2004. To solve the problem of excessive groundwater exploitation caused by large-scale demand for water resources by residents, China implemented the South-to-North Water Transfer Project at the end of 2014. After the middle route of the project was implemented, the demand for residential water shifted from groundwater exploitation to south-to-north water diversion; thus, preventing land subsidence to a certain extent. During 2015–2020, the land subsidence rate in 2020 was 99 mm/year, which was 21 mm/year lower than that in 2015. Although the land subsidence rate increased from 2015 to 2017, it showed a declining trend after 2017, whereas an overall decreasing trend was observed from 2015 to 2020.

Figure 14 shows monthly precipitation deformation during the study period. In Figure 14, it can be observed that rainfall is mainly concentrated in the summer months of May-August, and the rainfall in summer is higher than that in other seasons. On this basis, we combined surface deformation with rainfall trends and analyzed the relationship between them. During the concentrated rainfall period, there is an obvious rebound deformation phenomenon along the LOS direction. We discovered that higher rainfall from May to August 2006 reduced the need to use groundwater for farm irrigation, and, thus, land subsidence rate showed a gradually slowing trend from October 2006 to March of the following year. Meanwhile, rainfall in autumn and winter of the same year decreased, so that land subsidence in the spring of the following year showed intensification. This indicates that peoples' demand for groundwater decreases after rainfall, which slows down land subsidence to a certain extent. Ground settlement is negatively correlated with precipitation.

### *5.3. Relationship between Land Subsidence and Geological Structures and Faults in Beijing*

Beijing is located at the intersection of Yanshan, North China Plain, and Taihang Mountain fault. Due to its complex tectonic environment and active neo-tectonic movement, many active fault zones, including Huangzhuang-Gaoliying and Nankou-Sunhe in the northeast, Shunyi-Qianmen-Liangxiang, and Nanyuan-Tongxian, have been formed in the boundary area [65]. The sediments in Beijing are mainly distributed in the Beijing Plain and vary in thickness from a few meters to several hundred meters. The presence of a compressible layer is the elementary criterion of ground subsidence. The lithologic conditions and structural characteristics of Beijing provide an inner geological background for land subsidence, which mainly occurs in the quaternary strata. The sedimentary time, genetic type, lithology and thickness of the quaternary strata affect land subsidence [66]. Previous studies have shown that when the groundwater level declines in Beijing, the pore water pressure of the clayey aquifer decreases, and the effective stress in the soil increases, thus resulting in compression deformation and land subsidence [67].

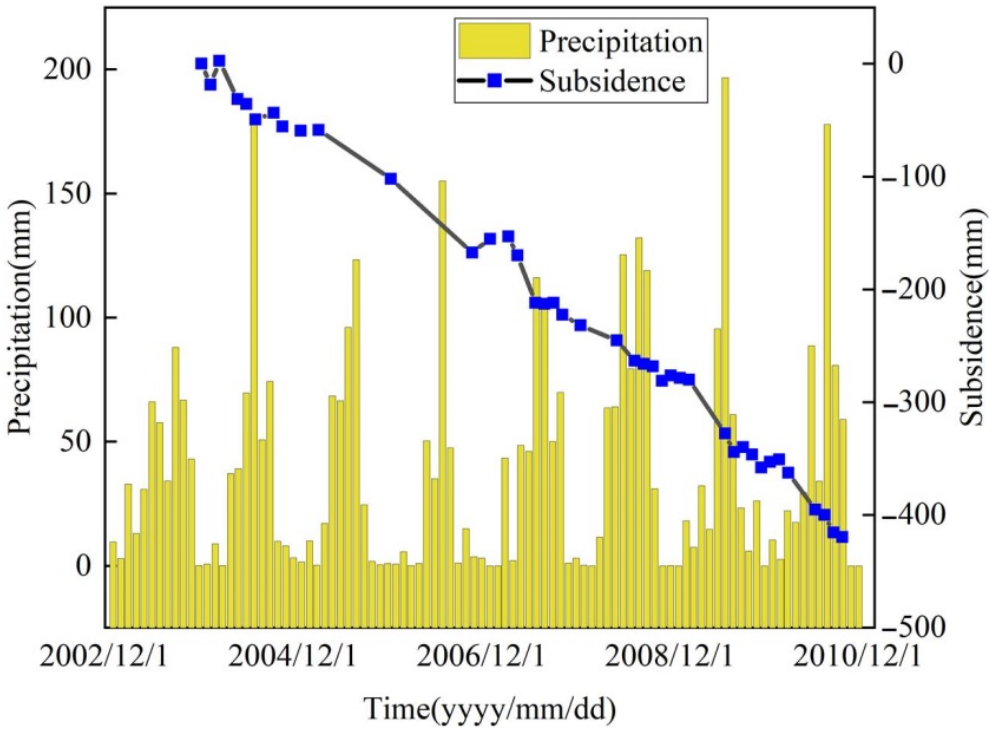


**Figure 14.** Changes in precipitation from 2003 to 2010.

Section 4.2 shows the feasibility of using a quadratic polynomial fitting algorithm and mean algorithm to supplement missing data required for land subsidence analysis. It not only reduces the cost of using other expensive satellite data, such as ALOS-2 and Radarsat-2, but also successfully reflects the changing trend of land subsidence in Beijing from 2010 to 2015. Moreover, the result obtained by the Mann-Kendall method was in good agreement with the analysis results. However, the quadratic polynomial fitting algorithm and mean algorithm are relatively simple. Therefore, it is necessary to combine groundwater change and the subsidence model to connect long-term time-series deformation in the future.

## 6. Conclusions

Using Beijing as the study area, we studied spatiotemporal evolution characteristics and their influencing factors for the time period from 2003 to 2020. First, 40 ENVISAT images and 90 Sentinel-1A/1B images were selected, and SBAS-InSAR technology was used to acquire LOS deformation rate charts and accumulated deformation charts during 2003–2010 and 2015–2020 in Beijing. We then analyzed the spatiotemporal variation characteristics of land subsidence during 2003–2010 and 2015–2020. This study provides significant deformation information for the Beijing area. Furthermore, the results of this study have important reference significance for stability analysis, large-scale engineering construction, urban planning and comprehensive utilization of land resources in Beijing. We can draw the following main conclusions from this study. Firstly, the distribution of land subsidence in Beijing was found to be uneven. The settlement is mainly located in the northeast and more stable in the middle. In the former stage, the maximum deformation rate was −128 mm/year, and the maximum cumulative deformation amount was −808 mm, which is located in Chaoyang. In the latter stage, the maximum deformation rate in Beijing was −135 mm/year, and the maximum cumulative deformation amount reached was −734 mm. Using GPS measurements, we demonstrated the reliability of our InSAR annual subsidence results. Secondly, modified surface deformation results were obtained by using the quadratic polynomial fitting method combined with GPS data to report on the evolutionary characteristics of surface subsidence during 2003–2020. The reported results are consistent with those obtained by the Mann-Kendall method. On the other hand, it

showed that, although the InSAR observation method is not strictly registered with GPS in time, the deformation trend was consistent, which further demonstrated the reliability of InSAR monitoring results. In addition, the calibrated long time-series was consistent with the three deformation stages of land subsidence evolution in Beijing. Thirdly, compared with other land use types, construction land is more prone to land subsidence and its influence on land subsidence is closely related to overexploitation of groundwater. Fourthly, overexploitation of groundwater can aggravate land subsidence. The implementation of the middle line project at the end of 2014 prevented land subsidence to a certain extent. In addition, during the concentrated rainfall period, there is an obvious rebound deformation phenomenon along the LOS direction. It shows that the seasonal variation in deformation is related to precipitation. Finally, geological factors show that when groundwater level declines in Beijing, the pore water pressure of the clayey aquifer decreases, and the effective stress in the soil increases, thus resulting in compression deformation and land subsidence. Therefore, land use type and precipitation have little influence on land subsidence. The change of groundwater level is the main influence factor of land subsidence.

**Author Contributions:** Conceptualization, S.Z. and Y.Z.; methodology, S.Z. and Y.Z.; software, Y.Z.; validation, Y.Z., J.Y., Q.F. and J.S.; writing—original draft preparation, Y.Z. and S.Z.; writing—review and editing, Q.F., J.S. and W.Z.; supervision, M.S. All authors have read and agreed to the published version of the manuscript.

**Funding:** This research was funded by the National Key Research and Development Program of China (2019YFC1509802, 2020YFC1512000); the National Natural Science Foundation of China (42074041,41731066); State Key Laboratory of Geo-Information Engineering (SKLGIE2019-Z-2-1); Shaanxi Natural Science Research Program (2020JM-227).

**Data Availability Statement:** ENVISAR ASAR datasets provided in the article is available at http://esar-ds.eo.esa.int/socat/ASA_IMS_1P, accessed on 12 January 2022. Sentinel-1A/1B data provided in the article is available at https://vertex.daac.asf.alaska.edu/, accessed on 20 January 2022. DEM provided in the study is available at https://earthexplorer.usgs.gov/, accessed on 12 January 2022. Groundwater provided in the article is available at http://swj.beijing.gov.cn/, accessed on 10 February 2022. Precipitation provided in the article is available at https://www.ncei.noaa.gov/maps-and-geospatial-products, accessed on 10 February 2022.

**Acknowledgments:** The author would like to thank ESA for providing sentinel-1A/1B, ENVISAT ASAR data. Thanks to NASA for the SRTM DEM elevation data. Thanks to Beijing Water Authority for the data of groundwater exploitation and groundwater depth. Thanks to GEE platform for providing Landsat data and land use and classification data. Thanks to NOAA for providing precipitation data.

**Conflicts of Interest:** The authors declare no conflict of interests.

## Appendix A

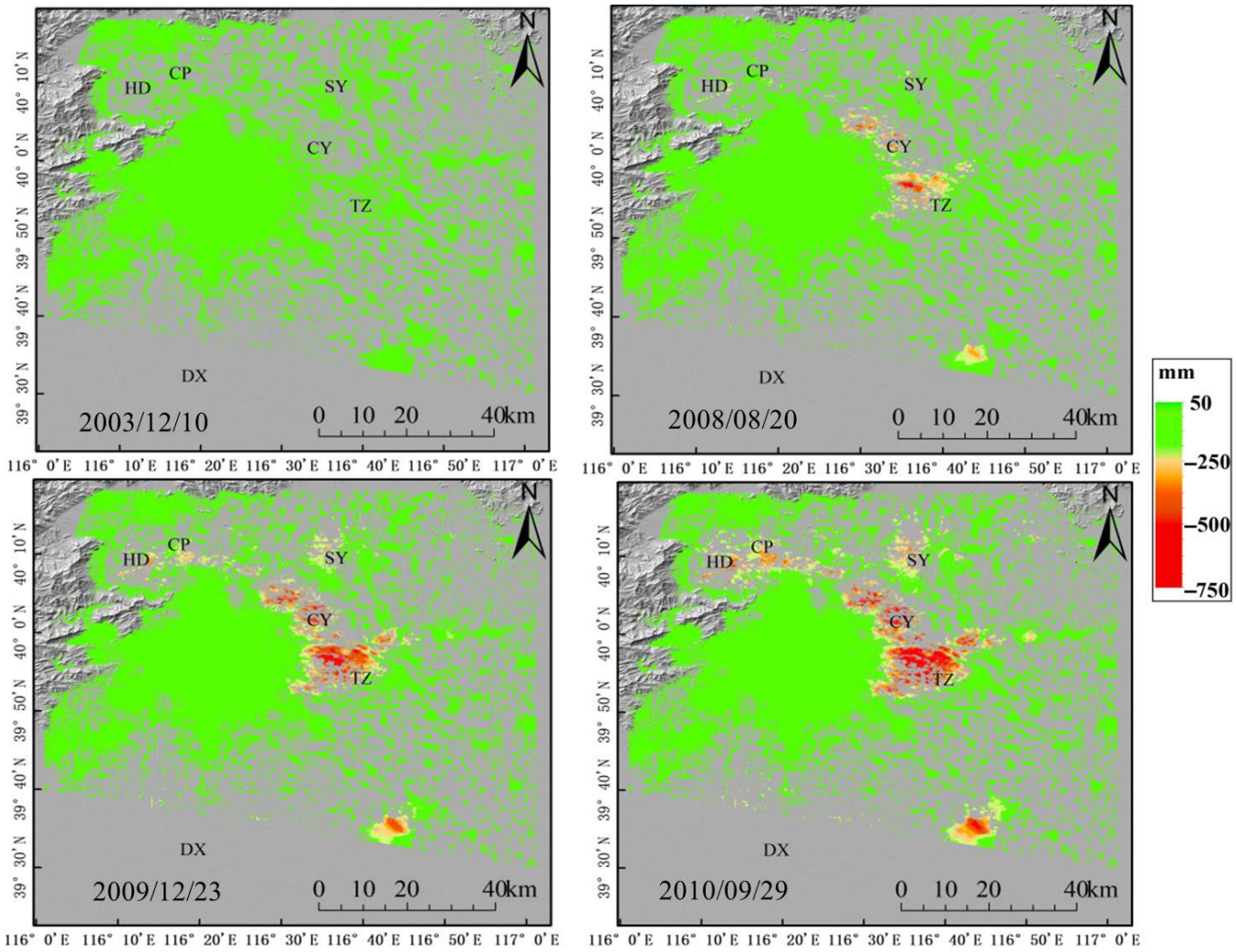


**Figure A1.** Cumulative time-series deformation in LOS from 2003 to 2010. CY: Chaoyang District, CP: Changping District, HD: Haidian District, SY: Shunyi District, and TZ: Tongzhou District.

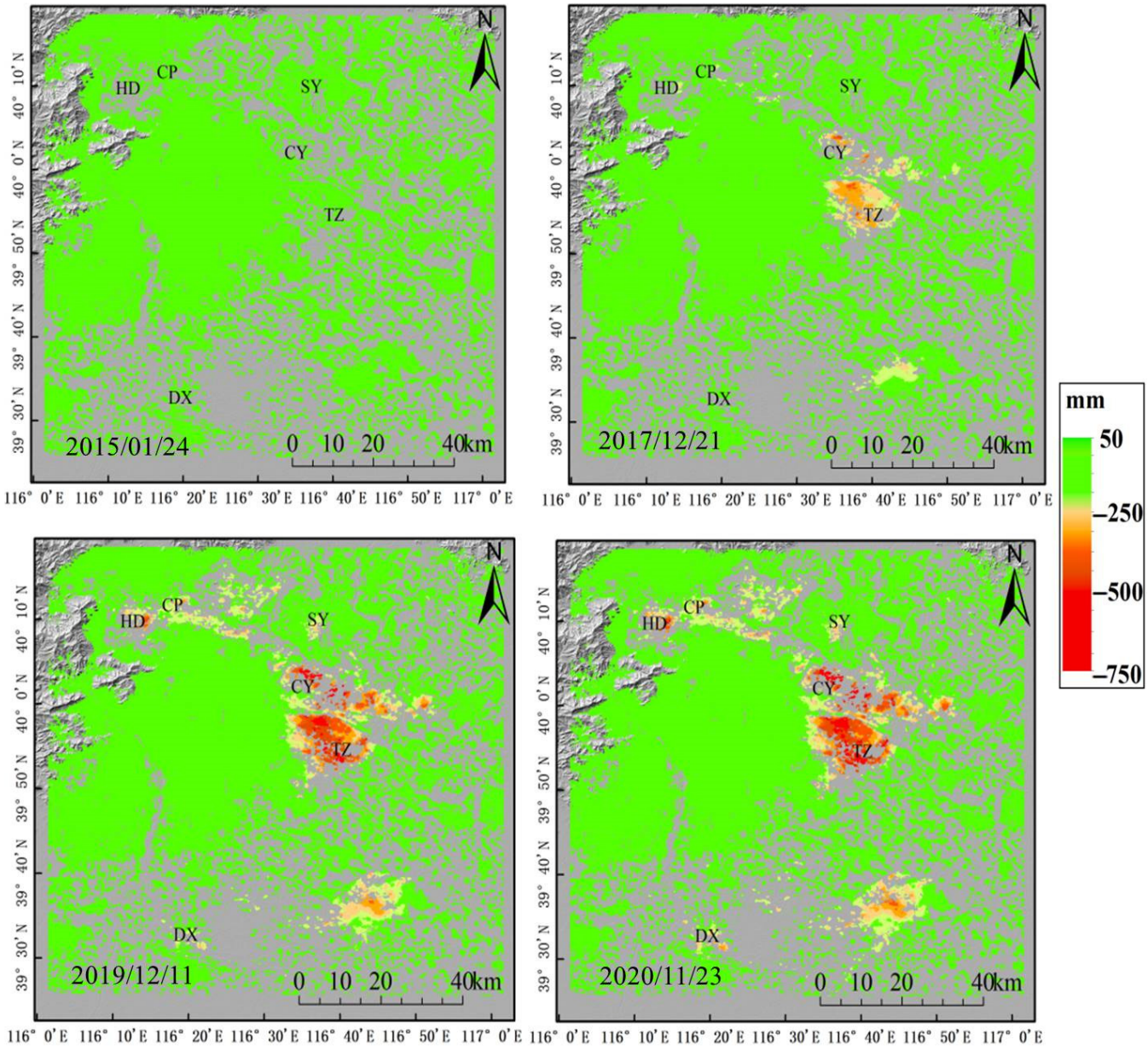


**Figure A2.** Cumulative time-series deformation along the LOS from 2015 to 2020. CY: Chaoyang District, CP: Changping District, HD: Haidian District, SY: Shunyi District, and TZ: Tongzhou District.

## References

1. Xu, Y.S.; Shen, S.L.; Cai, Z.Y.; Zhou, G.Y. The state of land subsidence and prediction approaches due to groundwater withdrawal in China. *Nat. Hazards* **2008**, *45*, 123–135. [CrossRef]
2. Chen, B.B.; Gong, H.L.; Li, X.J.; Lei, K.C.; Gao, M.L.; Zhou, C.F.; Ke, Y.H. Spatial–temporal evolution patterns of land subsidence with different situation of space utilization. *Nat. Hazards* **2015**, *77*, 1765–1783. [CrossRef]
3. Zhang, Y.Q.; Gong, H.L.; Gu, Z.Q.; Wang, R.; Li, X.J.; Zhao, W.J. Characterization of Land Subsidence Induced by Groundwater Withdrawals in the Plain of Beijing City, China. *Hydrogeol. J.* **2014**, *22*, 397–409. [CrossRef]
4. Bürgmann, R.; Hilley, G.; Ferretti, A.; Novali, F. Resolving Vertical Tectonics in the San Francisco Bay Area from Permanent Scatterer InSAR and GPS Analysis. *Geology* **2006**, *34*, 221–224. [CrossRef]
5. Osmanoğlu, B.; Sunar, F.; Wdowinski, S.; CabralCano, E. Time series analysis of InSAR data: Methods and trends. *Int. Soc. Photogramm. Remote Sens.* **2016**, *115*, 90–112. [CrossRef]
6. Yan, Y.; Doin, M.P.; Lopez-Quiroz, P.; Tupin, F.; Fruneau, B.; Pinel, V.; Trouvé, E. Mexico City subsidence measured by InSAR time series: Joint analysis using PS and SBAS approaches. *IEEE J. Sel. Top. Appl. Earth Obs. Remote Sens.* **2012**, *5*, 1312–1326. [CrossRef]
7. Hu, B.; Wang, H.S.; Jiang, L.M. Monitoring of the reclamation-induced ground subsidence in Macao (China) using the PSInSAR technique. *J. Cent. South Univ.* **2013**, *20*, 1039–1046. [CrossRef]

8. Li, Z.H.; Liu, J.N.; Xu, C.J. Error Analysis in InSAR Data Processing. *Geomat. Inf. Sci. Wuhan Univ.* **2004**, *29*, 72–76. (In Chinese)
9. Yan, W.; Ming-Sheng, L.; De-Ren, L.; Zi-Xin, W.; Zheng, F. Subsidence velocity retrieval from long-term coherent targets in radar interferometric stacks. *Chin. J. Geophys.* **2007**, *50*, 598–604. (In Chinese)
10. He, X.F.; Gao, Z.; Xiao, R.Y.; Luo, H.B.; Feng, C. Monitoring and analysis of subsidence along Lian-Yan railway using multitemporal Sentinel-1A InSAR. *Acta Geod. Et Cartogr. Sin.* **2021**, *50*, 600–611. (In Chinese)
11. Dai, K.; Liu, G.X.; Li, Z.H.; Li, T.; Yu, B.; Wang, X.W.; Singleton, A. Extracting Vertical Displacement Rates in Shanghai (China) with Multi-Platform SAR Images. *Remote Sens.* **2015**, *7*, 9542–9562. [CrossRef]
12. Perissin, D.; Wang, T. Time-Series InSAR Applications Over Urban Areas in China. *IEEE J. Sel. Top. Appl. Earth Obs. Remote Sens.* **2010**, *4*, 92–100. [CrossRef]
13. Heleno, S.I.; Oliveira, L.G.; Henriques, M.J.; Falcão, A.P.; Lima, J.N.; Cooksley, G.; Ferretti, A.; Fonseca, A.M.; Ferreira, J.P.; Fonseca, J.F. Persistent Scatterers Interferometry detects and measures ground subsidence in Lisbon. *Remote Sens. Environ.* **2011**, *115*, 2152–2167. [CrossRef]
14. Sousa, J.J.; Hooper, A.J.; Hanssen, R.F.; Bastos, L.C.; Ruiz, A.M. Persistent Scatterer InSAR: A comparison of methodologies based on a model of temporal deformation vs. spatial correlation selection criteria. *Remote Sens.* **2011**, *115*, 2652–2663. [CrossRef]
15. Wang, C.S.; Wang, X.S.; Xu, Y.P.; Zhang, B.C.; Jiang, M.; Xiong, S.T.; Zhang, Q.; Li, W.D.; Li, Q.Q. A new likelihood function for consistent phase series estimation in distributed scatterer interferometry. *IEEE Trans. Geosci. Remote. Sens.* **2022**, 1. [CrossRef]
16. Ferretti, A.; Prati, C.; Rocca, F. Permanent scatterers in SAR interferometry. *IEEE Trans. Geosci. Remote Sens.* **2001**, *39*, 8–20. [CrossRef]
17. Lu, Z.; Danskin, W. InSAR analysis of natural recharge to define structure of a groundwater basin, San Bernardino, California. *Geophys. Res. Lett.* **2001**, *28*, 2661–2664. [CrossRef]
18. Berardino, P.; Fornaro, G.; Lanari, R.; Sansosti, E. A New Algorithm for Surface Deformation Monitoring Based on Small Baseline Differential SAR Interferograms. *IEEE Trans. Geosci. Remote Sens.* **2002**, *40*, 2375–2383. [CrossRef]
19. Lanari, R.; Mora, O.; Manunta, M.; Mallorquí, J.J.; Berardino, P.; Sansosti, E. A small-baseline approach for investigating deformations on full-resolution differential SAR interferograms. *IEEE Trans. Geosci. Remote Sens.* **2004**, *42*, 1377–1386. [CrossRef]
20. Mora, O.; Mallorqui, J.J.; Broquetas, A. Linear and nonlinear terrain deformation maps from a reduced set of interferometric SAR images. *IEEE Trans. Geosci. Remote Sens.* **2003**, *41*, 2243–2253. [CrossRef]
21. Shi, M.; Gong, H.L.; Gao, M.L.; Chen, B.B.; Zhang, S.K.; Zhou, C.F. Recent Ground Subsidence in the North China Plain, China, Revealed by Sentinel-1A Datasets. *Remote Sens.* **2020**, *12*, 3579. [CrossRef]
22. Yuan, M.Z.; Li, M.; Liu, H.; Lv, P.; Li, B.; Zheng, W. Subsidence Monitoring Base on SBAS-InSAR and Slope Stability Analysis Method for Damage Analysis in Mountainous Mining Subsidence Regions. *Remote Sens.* **2021**, *13*, 3107. [CrossRef]
23. Zhou, L.; Guo, J.M.; Li, X. Monitoring and analyzing surface subsidence based on SBAS-InSAR in Beijing region, China. In Proceedings of the International Conference on Intelligent Earth Observing and Applications, Guilin, China, 9 December 2015.
24. Li, Y.S.; Zhang, J.F.; Li, Z.H.; Luo, Y. Land Subsidence in Beijing City from InSAR Time Series Analysis with Small Baseline Subset. *Geomat. Inf. Sci. Wuhan Univ.* **2013**, *38*, 1374–1377. (In Chinese)
25. Pan, C.; Jiang, L.M.; Sun, Q.S.; Jiang, Y.N. Monitoring and Analyzing Chengdu Ground Subsid-ence Based on InSAR Technology by Using Sentinel-1 Radar Image. *J. Geod. Geodyn.* **2020**, *40*, 198–203.
26. Zhou, C.; Gong, H.; Chen, B.; Zhou, F.; Duan, G.; Gao, M.; Lu, W. Land Subsidence under Different Land Use in the Eastern Beijing Plain, China 2005–2013 revealed by InSAR timeseries analysis. *GISci. Remote Sens.* **2016**, *53*, 671–688. [CrossRef]
27. Du, Z.; Ge, L.; Ng, A.H.M.; Xiaojing, L.; Li, L. Mapping land subsidence over the eastern Beijing city using satellite radar interferometry. *Int. J. Digit. Earth* **2018**, *11*, 504–519. [CrossRef]
28. Liu, L.M.; Yu, J.; Chen, B.B.; Zhu, F.; Duan, G.Y.; Gao, M.L.; Lu, W. Urban subsidence monitoring by SBAS-InSAR technique with multi-platform SAR images: A case study of Beijing Plain, China. *Eur. J. Remote Sens.* **2020**, *53*, 141–153. [CrossRef]
29. Muhetaer, N.; Yu, J.; Wang, Y.B.; Yue, J. Temporal and Spatial Evolution Characteristics Analysis of Beijing Land Subsidence Based on InSAR. In Proceedings of the 3rd International Forum on Geoscience and Geodesy, Shenyang, China, 13–15 November 2020; Volume 658, pp. 13–15.
30. Yang, Q.; Ke, Y.H.; Zhang, D.Y.; Chen, B.B.; Gong, H.L.; Lv, M.Y.; Zhu, L.; Li, X.J. Multi-Scale Analysis of the Relationship between Land Subsidence and Buildings: A Case Study in an Eastern Beijing Urban Area Using the PS-InSAR Technique. *Remote Sens.* **2018**, *10*, 1006. [CrossRef]
31. Ng, A.H.M.; Ge, L.L.; Li, X.J.; Zhang, K. Monitoring ground deformation in Beijing, China with persistent scatterer SAR interferometry. *J. Geod.* **2011**, *86*, 375–392. [CrossRef]
32. Hu, L.Y.; Dai, K.R.; Xing, C.Q.; Li, Z.; Tomás, R.; Clark, B.; Shi, X.; Chen, M.; Zhang, R.; Qiu, Q.; et al. Land subsidence in Beijing and its relationship with geological faults revealed by Sentinel-1 InSAR observations. *Int. J. Appl. Earth Obs. Geoinf.* **2019**, *82*, 101886. [CrossRef]
33. Zhou, C.F.; Gong, H.L.; Chen, B.B.; Li, X.; Li, J.; Wang, X.; Gao, M.; Si, Y.; Guo, L.; Shi, M.; et al. Quantifying the contribution of multiple factors to land subsidence in the Beijing Plain, China with machine learning technology. *Geomorphology* **2019**, *335*, 48–61. [CrossRef]
34. Samsonov, S.V.; D'Oreye, N.; González, P.J.; Tiampo, K.F.; Ertolahti, L.; Clague, J.J. Rapidly accelerating subsidence in the Greater Vancouver region from two decades of ERS ENVISAT RADARSAT-2 DInSAR measurements. *Remote Sens. Environ.* **2014**, *143*, 180–191. [CrossRef]

35. Pepe, A.; Zhao, Q.; Bonano, M.; Lu, Z.; Zhou, Y. The study of the deformation time evolution in coastal areas of Shanghai:a joint C/X-band SBAS-DInSAR analysis. In Proceedings of the Name of the 2015 IEEE International Geoscience and Remote Sensing Symposium (IGARSS), Milan, Italy, 26–31 July 2015; pp. 306–309.
36. Gao, M.L.; Gong, H.L.; Chen, B.B.; Zhou, C.F.; Chen, W.F.; Liang, Y.; Shi, M.; Si, Y. InSAR time-series investigation of long-term ground displacement at Beijing Capital International Airport, China. *Tectonophysics* **2016**, *691*, 271–281. Available online: http://geodata.geoscience.cn/cjy/cjy.action (accessed on 14 January 2022). [CrossRef]
37. Wang, Z.; Cai, X.; Yan, J.; Wang, J.; Liu, Y.; Zhang, L. Using the integrated geophysical methods detecting active faults: A case study in Beijing, China. *J. Appl. Geophys.* **2018**, *156*, 82–91. [CrossRef]
38. Yang, Y.; Jia, S.M.; Wang, H.G. The Status and Development of Land Subsidence in Beijing Plain. *Shanghai Geol.* **2010**, *31*, 23–27.
39. Yang, Y.; Jia, S.M.; Wang, H.G.; Zhou, Y. Analysi s on impact of land subsidence on planned new cities in Beijing. *City Plan. Rev.* **2013**, *37*, 67–71. (In Chinese)
40. Yang, J.; Huang, X. The 30 m annual land cover dataset and its dynamics in China from 1990 to 2019. *Earth Syst. Sci. Data* **2021**, *13*, 3907–3925. [CrossRef]
41. Zhu, J.J.; Li, Z.W.; Hu, J. Research Progress and Methods of InSAR for Deformation Monitoring. *Acta Geod. Et Cartogr. Sinica* **2017**, *46*, 1717–1733.
42. Yang, C.S.; Zhang, Q.; Zhao, C.Y.; Ji, L.Y. Small Baseline Subset InSAR Technology Used in Datong Basin Ground Subsidence, Fissure and Fault Zone Monitoring. *Geomat. Inf. Sci. Wuhan Univ.* **2014**, *39*, 945–950.
43. Song, Y.F.; Liu, G.X.; Zhang, R. Monitoring Significant Ground Subsidence by Using New Small Baseline Subset Multiple Temporal InSAR Approach. *Remote Sens. Inf.* **2016**, *31*, 84–88.
44. Golub, G.H.; VanLoan, C.F. *Matrix Computation*; Johns Hopkins University Press: Baltimore, MD, USA, 1996.
45. Zhu, Y.X.; Feng, L.P.; Jia, X.L.; Zhang, Q.H.; Ruan, R.G. The PPP precision analysis based on BDS regional navigation system. *Acta Geod. Et Cartogr. Sin.* **2015**, *44*, 377–383.
46. Liu, Y. *GAMIT/GLOBK Installation and Application Based on Linux System*; Beijing Surveying and Mapping: Beijing, China, 2014; pp. 30–33.
47. Liu, X.W.; Pu, D.X.; Gao, X.; Zhang, S.Y.; Xia, D.H. High Precision GPS/BDS Data Processing and Precision Contrast Analysis Based on GAMIT10.61. *GNSS World China* **2018**, *43*, 77–83.
48. Zhang, S.C.; Wang, Q.Y.; Liu, Q.; Zhang, C.L.; He, Y.F.; Zhao, G.S. Analysis of precision relative positioning accuracy of BDS by GAMIT. *Sci. Surv. Mapp.* **2018**, *43*, 92–97.
49. DONG, D.; HERRING, T.A.; KING, R.W. Estimating regional deformation from a combination of space and terrestrial geodetic data. *J. Geod.* **1998**, *72*, 200–214. [CrossRef]
50. Sun, F.L.; Song, S.L.; Zhu, W.Y.; Zheng, Z.Y. Utilizing GLOBK to Achieve Weekly Comprehensive Solution of GPS. *GNSS World China* **2013**, *38*, 61–65.
51. Wang, Y.; Ge, D.Q.; Zhang, L.; Li, M.; Guo, X.F.; Wang, Y. Inter-comparison and time series fusion of ascending and descending PSInSAR data for land subsidence monitoring. *Remote Sens. Land Resour.* **2014**, *26*, 125–130.
52. Dai, K.R.; Zhuo, G.C.; Xu, Q.; LI, Z.; LI, W.; Guan, W. Tracing the Pre-failure Two-dimensional Surface Displacements of Nanyu Landslide, Gansu Province with Radar Interferometry. *Geomat. Inf. Sci. Wuhan Univ.* **2019**, *44*, 1778–1786.
53. Zhang, J.J.; Zhang, H.X.; Zhang, M.S.; Tao, H.; Dong, Y.; Xu, C.M. Study on the seepage deformation induce ground fissures caused and subsidence in Xi'an. *J. Eng. Geol.* **2018**, *26*, 301–309.
54. Zhang, Y.; Xue, Y.Q.; Wu, J.C.; Wang, H.; He, J. Mechanical modeling of aquifer sands under long-term groundwater withdrawal. *Eng. Geol.* **2012**, *125*, 74–80. [CrossRef]
55. Tosi, L.; Teatini, P.; Carbognin, L.; Brancolini, G. Using high resolution data to reveal depth-dependent mechanisms that drive land subsidence: The venice coast, Italy. *Tectonophysics* **2009**, *474*, 271–284. [CrossRef]
56. Zhu, L.; Gong, H.L.; Li, X.J.; Wang, R.; Chen, B.; Dai, Z.; Teatini, P. Land subsidence due to groundwater withdrawal in the northern Beijing plain, China. *Eng. Geol.* **2015**, *193*, 243–255. [CrossRef]
57. Chen, M.; Tomas, R.; Li, Z.H.; Motagh, A.; Li, T.; Hu, L.Y.; Gong, H.L.; Li, X.J.; Yu, J.; Gong, X.L. Imaging Land Subsidence Induced by Groundwater Extraction in Beijing (China) Using Satellite Radar Interferometry. *Remote Sens.* **2016**, *8*, 468. [CrossRef]
58. Chen, B.B.; Gong, H.L.; Li, X.J.; Lei, K.C.; Zhang, Y.Q.; Li, J.W.; Gu, Z.Q.; Dang, Y.N. Spatial-temporal Characteristics of Land Subsidence Corresponding to Dynamic Groundwater Funnel in Beijing Municipality, China. *Chin. Geogr. Science* **2011**, *21*, 753–764. [CrossRef]
59. Zhou, C.D.; Gong, H.L.; Chen, B.B.; Li, J.W.; Gao, M.L.; Zhu, F.; Chen, W.F.; Liang, Y. InSAR time-series analysis of land subsidence under different landuse types in the eastern Beijing plain, China. *Remote Sens.* **2017**, *9*, 380. [CrossRef]
60. Zhou, C.F.; Gong, H.L.; Chen, B.B.; Gao, M.L.; Cao, Q.; Cao, J.; Duan, L.; Zuo, J.J.; Shi, M. Land Subsidence Response to Different Land Use Types and Water Resource Utilization in Beijing-Tianjin-Hebei, China. *Remote Sens.* **2020**, *12*, 457. [CrossRef]
61. Zhou, C.D.; Gong, H.L.; Zhang, Y.Q.; Duan, G.Y. The Influence of Building Load to Land Subsidence in Beijing Plain based on PS-InSAR and GIS. *J. Geo-Inf. Sci.* **2016**, *18*, 1551–1562.
62. Solari, L.; Ciampalini, A.; Raspini, F.; Bianchini, S.; Moretti, S. PSInSAR Analysis in the Pisa Urban Area (Italy): A Case Study of Subsidence Related to Stratigraphical Fac-tors and Urbanization. *Remote Sens.* **2016**, *8*, 120. [CrossRef]
63. Guo, H.P.; Li, W.P.; Wang, L.Y.; Chen, Y.; Zang, X.S.; Wang, Y.L.; Zhu, J.Y.; Bian, Y.Y. Present situation and research prospects of the land subsidence driven by groundwater levels in the North China Plain. *Hydrogeol. Eng. Geol.* **2021**, *48*, 162–171.

64. Long, D.; Yang, W.T.; Scanlon, B.R.; Zhao, J.S.; Liu, D.G.; Burek, P.; Pan, Y.; You, L.Z.; Wada, Y. South-to-North Water Diversion stabilizing Beijing's groundwater levels. *Nat. Commun.* **2020**, *11*, 3665. [CrossRef]
65. Chen, B.; Gong, H.; Li, X.; Lei, K.; Zhu, L.; Gao, M.; Zhou, C. Characterization and causes of land subsidence in Beijing, China. *Int. J. Remote Sens.* **2017**, *38*, 808–826. [CrossRef]
66. Zheng, J.R.; Gong, H.L.; Li, Q.Y.; Cui, Y.Z.; Chen, B.B. The Control Factors on Subsidence of Beijing Plain Area in 2003–2009 Based on PS-InSAR Technology. *Bull. Surv. Mapp.* **2014**, *12*, 40–43.
67. Karen, M.W.; Yehuda, B.; David, T.S. Satellite Interferometric Observations of Displacements Associated with Seasonal Groundwater in the Los Angeles Basin. *J. Geophys. Res. Atmos.* **2002**, *107*, 265–296.